

Binding and Exchange Reactions of Hydrogen Isotopes on Surfaces of Dispersed Pt Nanoparticles

Samuel L. Leung, David Hibbitts, Mónica García-Diéguez, and Enrique Iglesia*



Cite This: *J. Phys. Chem. C* 2022, 126, 3923–3938



Read Online

ACCESS |



Metrics & More



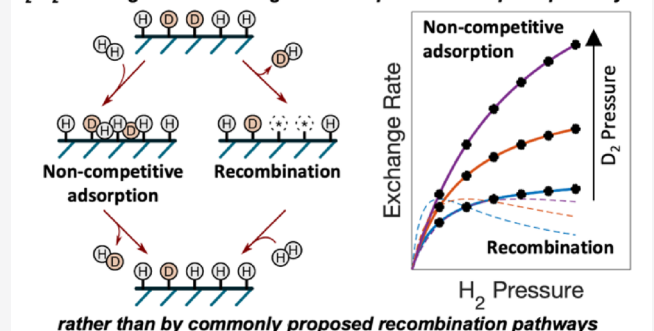
Article Recommendations



Supporting Information

ABSTRACT: H_2 – D_2 isotopic equilibration is often used to assess the involvement and reversibility of H_2 dissociative chemisorption steps during hydrogenation surface catalysis under the premise that exchange turnovers require recombinative desorption of adatoms (H^* , D^*). Experimental and theoretical evidence reported here show instead that exchange occurs via non-competitive adsorption mechanisms that circumvent recombinative desorption steps at temperatures of catalytic relevance (<700 K) and that H_2 and D_2 adsorption enthalpies are similar, leading to equilibrium isotope effects near unity (0.7–1.0) on dispersed Pt nanoparticles. The kinetic effects of H_2 and D_2 pressures on exchange rates at 300–700 K are accurately described by elementary steps involving the non-competitive adsorption of H_2 (or D_2) and its reaction with D^* (or H^*), mediated via local displacements of adatoms to alternate binding sites in H^*/D^* adlayers but without requiring their intervening endothermic recombinative desorption. Recombination ($H^* + D^*$) routes become prevalent only above 700 K, leading to different kinetic trends with H_2/D_2 pressures and to higher activation barriers (78 vs 32 kJ mol^{−1}) than for the single-site non-competitive adsorption routes that prevail at lower temperatures. Such conclusions are consistent with density functional theory (DFT) calculations on 4×4 Pt(111) models at saturation coverages (1 H^*/Pt_s), which show that barriers for single-site metalocycle mechanisms (205 kJ mol^{−1}) are much larger than those for routes involving H_2 or D_2 dissociation on “spaces” created by displacements of D^*/H^* adatoms (55 kJ mol^{−1}) and the concomitant local supersaturation of the Pt surface. Such pathways weaken the binding of H^* (or D^*) at such locations, thus enabling the facile desorption and exchange of H_2 and D_2 under conditions that would otherwise preclude the measured rates of exchange events. Pt₂₀₁ nanoparticle models allow greater adlayer relaxation and supramonolayer H^* coverages and lead to even lower DFT-derived barriers for non-competitive adsorption routes (27 kJ mol^{−1} at 1.44 H^*/Pt_s). Recombination routes exhibit higher barriers and become the predominant exchange pathways above 700 K; for reactions requiring such temperatures, exchange rates can provide a reliable assessment of the reversibility of dihydrogen dissociation events.

H_2 – D_2 exchange occurs through non-competitive adsorption pathways...



rather than by commonly proposed recombination pathways

1. INTRODUCTION

Isotopic tracer experiments and the analysis of kinetic effects of isotopic substitution are essential tools in discerning among plausible mechanisms of chemical transformations in surface catalysis. These methods are often used to assess the identity, reversibility, and kinetic relevance of elementary steps without disturbing the nature of reactants and products or the chemical steady state, thus providing direct mechanistic details, albeit often in difficult-to-interpret forms. The isotopic identity of atoms can affect the chemical reactivity of the bonds being cleaved or formed; it can also change the thermodynamic properties of molecules and the equilibrium constants for their chemical interconversions.¹ The ratio of reaction rates or rate constants for a molecule with the most abundant isotope relative to those of its isotopologues is denoted as a kinetic isotope effect (KIE), while the corresponding ratio in their equilibrium constants is known as a thermodynamic isotope effect (TIE). These effects arise from the different mass of each

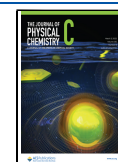
isotopologue and the effects of the isotopic atom on the vibrational frequency in the bonds that contain them in reactants, products, and transition states.^{2,3} As a result, these methods can be used to assess the involvement of specific bonds, especially for hydrogen and deuterium atoms, in kinetically relevant and quasi-equilibrated steps within a sequence of elementary steps,^{3–6} as shown previously for many catalytic reactions.^{7–18}

Isotopic labels can be used to “trace” the fate of atoms and the molecules that contain them through reaction networks,

Received: October 20, 2021

Revised: January 9, 2022

Published: February 17, 2022



thus probing the reversibility of steps that form or cleave chemical bonds that include the isotope;^{19,20} these methods are broadly used in surface catalysis.^{6,7,21–24} H₂–D₂ isotopic exchange, in particular, is often used to assess the reversibility of H₂ dissociation steps on surfaces in catalytic hydrogenation–dehydrogenation events



These experiments and interpretations, however, implicitly assume that isotopic scrambling events occur *only* via the dissociative adsorption and recombinative desorption reactions represented in eqs 1–3; such pathways are denoted here as the “recombinative desorption” mechanism. Isotopic exchange between H₂ and D₂ and para–ortho hydrogen interconversion reactions were previously examined on Pt wires under high-vacuum conditions; these studies concluded that single-site exchange events between H₂ and bound D* adatoms (and D₂ and H* adatoms) occur, possibly without requiring surface-mediated dissociation of H–H bonds in H₂, even below 200 K.²⁵ Similar conclusions were reached by Christmann et al. using H₂ and D₂ thermal desorption studies;²⁶ such pathways have also been proposed on other metals (Ni, Cu, Ag, Au).^{27–32} These studies, however, did not provide unequivocal kinetic evidence for such mechanisms at the pressures and temperatures relevant for catalytic turnovers; as a result, such conclusions are seldom cited in later studies that exploit such methods to assess the reversibility of H₂ dissociation events (eqs 1–3) during catalysis. These previous H₂–D₂ exchange studies also did not place the proposed exchange routes firmly within the context of the thermodynamics of H₂ and D₂ chemisorption on surfaces, which have been treated independently in later studies (e.g., Pt^{33–39}).

This study addresses the kinetics of H₂–D₂ isotopic exchange on Pt-based catalysts and the magnitude of H₂/D₂ TIEs under conditions of catalytic relevance. H₂ and D₂ chemisorption isotherms obtained at 523–673 K (10^{−4} to 10¹ kPa H₂ or D₂; 0.1–0.8 monolayer coverages) are nearly identical at each temperature, reflecting TIE values near unity. These TIE values depend very weakly on temperature, consistent with dissociative chemisorption enthalpies for H₂ and D₂ on Pt surfaces that differ only by 4.2 ± 1.2 kJ mol^{−1}; these enthalpies can be used to calculate equilibrium coverages of H* and D* for H₂–D₂ mixtures at other temperatures.

H₂–D₂ exchange rates on Pt catalysts at 383 K increase monotonically with H₂ and D₂ pressure (5–80 kPa H₂, 5–80 kPa D₂). Exchange rates are also nearly identical when H₂ and D₂ pressures are switched, in contrast with the rate differences expected from TIE values at 383 K (0.6 ± 0.2). These kinetic data are inconsistent with the recombinative desorption mechanism (eqs 1–3) as the predominant route for H₂–D₂ isotopic exchange. An alternate route, in which H₂ adsorbs non-competitively with an equilibrated H*/D* adlayer and reacts with D* (and D₂ reacts with H*),^{25,27–32} is, however, consistent with all experimental and theoretical evidence. These reactions (H₂–D* and D₂–H*) provide an alternate reaction pathway that leads to H*/D* surface compositions set by the kinetics of exchange events instead of the thermodynamics of H₂ and D₂ dissociative adsorption. H₂–D* and D₂–H* reactions are shown to exhibit KIE values (defined as the ratio of rate constants for H₂–D* and D₂–H* reactions) near

unity (1.1 ± 0.3). Such routes, denoted here as “non-competitive adsorption” pathways, are consistent with the absence of a maximum in exchange rate near equimolar H₂–D₂ compositions. These exchange reactions, which resemble in the functional forms of the rate equation those for Eley–Rideal kinetics,³¹ remain the dominant pathway at all temperatures below 700 K (5–40 kPa, total H₂/D₂ pressure).

The kinetic behavior of H₂–D₂ exchange cannot distinguish various structurally distinct H₂–D* and D₂–H* reaction mechanisms and the interactions involved at the transition state. Density functional theory (DFT) calculations on flat Pt(111) surfaces and 201-atom Pt nanoparticles show that these exchange events are mediated by dissociation of H₂ or D₂ on Pt surfaces at spaces that form via the displacement of single H* and D* adatoms to alternate binding modes within the equilibrated mobile H*/D* adlayers prevalent at these temperatures (383–700 K); such pathways do not require the desorption of a H* or a D* atom for exchange turnovers to occur. H₂–D₂ isotopic exchange thus occurs via pathways that circumvent the recombinative desorption of H* and D* (the reverse of eqs 1–3). Consequently, exchange rates cannot be used to unequivocally demonstrate reversibility of H₂ adsorption (eqs 1–3) under conditions of catalytic hydrogenation/dehydrogenation reactions.

2. METHODS

2.1. Catalyst Synthesis Methods. Pt nanoparticles dispersed on SiO₂ (0.2% wt, Pt/SiO₂-A) were prepared using strong electrostatic adsorption methods⁴⁰ that exploit interactions between SiO₂ surfaces that are negatively charged at the prevalent solution pH (11.4) and aqueous cationic Pt precursors ([Pt(NH₃)₄](NO₃)₂; 99.99% metals basis, Alfa Aesar) to form well-dispersed strongly bound precursors. SiO₂ (Davisil, grade 62, Sigma-Aldrich) was treated before Pt deposition in flowing air (0.83 cm³ g^{−1} s^{−1}; zero grade, Praxair) while ramping from ambient temperature to 1073 K (0.083 K s^{−1}), holding for 5 h, and cooling to ambient temperature. [Pt(NH₃)₄](NO₃)₂ (0.0060 g) and SiO₂ (1.5 g) were then added to 25 cm³ of a 0.4 M NH₄OH solution, prepared by diluting a 25% solution NH₄OH (Sigma-Aldrich) in deionized (DI) water (>18.0 MΩ cm resistivity) and stirring for 2 h. The solids were filtered and rinsed three times with DI water (100 cm³ g^{−1}) and treated overnight in ambient stagnant air at 368 K. Samples were then treated in flowing air (1.67 cm³ g^{−1} s^{−1}; zero grade, Praxair) while heating from ambient temperature to 873 K (at 0.083 K s^{−1}) and holding for 3 h before again cooling to ambient temperature. This was followed by treatment in flowing H₂ (1.67 cm³ g^{−1} s^{−1}; 99.999% UHP; Praxair) while ramping to 1073 K (at 0.083 K s^{−1}) and holding for 2 h. After cooling, the sample was exposed to flowing 2% mol O₂ (balance He) (1.67 cm³ g^{−1} s^{−1}; certified grade, Praxair) for 0.5 h at ambient temperature. This O₂ treatment is intended to passivate Pt nanoparticle surfaces, thus avoiding exothermic oxidation processes upon contact with ambient air. A second sample of Pt/SiO₂ (0.2% wt, Pt/SiO₂-B) was prepared using similar steps but treated in flowing air and H₂ at 623 K instead of 873 K to avoid additional structural changes caused by exposure to higher temperatures.

Pt nanoparticles dispersed on γ-Al₂O₃ (1% wt, Pt/γ-Al₂O₃-A) were prepared by incipient wetness impregnation. γ-Al₂O₃ (Sasol, CATALOX SBA 200) was treated before Pt deposition in flowing air (0.83 cm³ g^{−1} s^{−1}; zero grade, Praxair) while ramping to 1073 K (0.083 K s^{−1}) and holding for 5 h. An

aqueous solution of H_2PtCl_6 (2.4% wt in H_2O) was prepared by diluting an aqueous solution of H_2PtCl_6 (8% wt in H_2O ; Sigma-Aldrich) in DI H_2O ($>18.0 \text{ M}\Omega \text{ cm}$ resistivity) and added dropwise to $\gamma\text{-Al}_2\text{O}_3$ ($0.86 \text{ cm}^3 \text{ g}^{-1} \gamma\text{-Al}_2\text{O}_3$). The sample was treated in ambient air at 368 K overnight and then in flowing air ($1.67 \text{ cm}^3 \text{ g}^{-1} \text{ s}^{-1}$; zero grade; Praxair) by heating from ambient temperature to 873 K (at 0.083 K s^{-1}) and holding for 3 h before cooling to ambient temperature. This procedure was followed by treatment in flowing H_2 ($1.67 \text{ cm}^3 \text{ g}^{-1} \text{ s}^{-1}$; 99.999% UHP; Praxair) while heating to 1073 K (at 0.083 K s^{-1}) and holding for 2 h. After cooling, the sample was treated in a 2% O_2/He stream (certified grade; Praxair) for 0.5 h at ambient temperature in order to passivate the surfaces of the Pt nanoparticles.

Pt/SiO_2 (5% wt, $\text{Pt}/\text{SiO}_2\text{-C}$) and $\text{Pt}/\gamma\text{-Al}_2\text{O}_3$ (1.6% wt, $\text{Pt}/\gamma\text{-Al}_2\text{O}_3\text{-B}$) samples were also prepared and used in H_2 and D_2 uptake experiments to measure TIE values. $\text{Pt}/\gamma\text{-Al}_2\text{O}_3\text{-B}$ was prepared as reported previously.³³ $\text{Pt}/\text{SiO}_2\text{-C}$ was prepared by incipient wetness impregnation of SiO_2 (Cabosil, HS-5, $310 \text{ m}^2 \text{ g}^{-1}$) with an aqueous solution of $\text{Pt}(\text{NH}_3)_4(\text{NO}_3)_2$ (Alfa Aesar, CAS 20634-12-2). This sample was treated in flowing dry air (99.99%, $0.8 \text{ cm}^3 \text{ g}^{-1} \text{ s}^{-1}$, Praxair) at 673 K (0.033 K s^{-1}) for 3 h and then treated in flowing 9% H_2/He (Praxair, $1.67 \text{ cm}^3 \text{ g}^{-1} \text{ s}^{-1}$) by heating from ambient temperature to 773 K at 0.033 K s^{-1} and holding for 3 h. It was then passivated at ambient temperature by exposure to flowing 0.5% O_2/He (Praxair, certified grade, $0.05 \text{ cm}^3 \text{ g}^{-1} \text{ s}^{-1}$) for 1 h before contact with ambient air.

Pt black (Strem Chemicals, a $22.7 \text{ m}^2 \text{ g}^{-1}$ nominal surface area) was used as received and treated before $\text{H}_2\text{-D}_2$ kinetic experiments, as described below.

2.2. Measurement of H_2 and D_2 Chemisorption Isotherms. The dispersion values, defined as the ratio of the number of exposed Pt sites to the total number of Pt atoms, for $\text{Pt}/\text{SiO}_2\text{-A}$, $\text{Pt}/\text{SiO}_2\text{-B}$, and $\text{Pt}/\gamma\text{-Al}_2\text{O}_3\text{-A}$ samples were measured from H_2 chemisorption uptakes. Samples (ca. 1 g) were treated in flowing H_2 (99.999% UHP; Praxair; $0.33 \text{ cm}^3 \text{ g}^{-1} \text{ s}^{-1}$) while at 673 K (0.083 K s^{-1}) for 1 h and then evacuated ($<10^{-5} \text{ Pa}$) at this temperature for 1 h. The sample was then cooled in vacuum to 373 K. H_2 chemisorption uptakes were measured at 1–40 kPa H_2 and 373 K. Saturation uptakes were determined by linear extrapolation of the uptakes to zero H_2 pressure. Nanoparticle diameters were calculated using the following relations⁴¹

$$d = \frac{f_{\text{shape}} N_{\text{M}} v_{\text{m}} \theta_{\text{sat}}}{2 N_{\text{H}_2} a_{\text{m}}} \quad (4)$$

$$\theta_{\text{sat}} = \text{H}/\text{Pt}_{\text{s}} = 1 + \alpha(d^{-1}) + \beta(d^{-2}) \quad (5)$$

Here, d is the diameter of the particle; f_{shape} is a shape factor (6 for a hemispherical particle); N_{M} is the total number of metal atoms; N_{H_2} is the number of H_2 molecules dissociated onto the surface; v_{m} and a_{m} are the volume and surface area of a Pt atom (calculated from the bulk density of Pt, 21.45 g cm^{-3});⁴² and α (0.0364) and β (0.735) are empirical parameters specific for Pt.⁴¹ Pt_{s} denotes atoms on the metal surface. This system of equations (eqs 4 and 5) can be solved iteratively to obtain the particle diameter (d) and saturation coverage (θ_{sat}) in a manner that corrects for supra-stoichiometric H^* coverages that arise from the binding of multiple H atoms on corner and edge sites on small metal nanoparticles.⁴¹

H_2 and D_2 chemisorption uptakes (523–673 K at 0.1–30 kPa H_2 or D_2) were also measured on $\text{Pt}/\text{SiO}_2\text{-C}$ and $\text{Pt}/\gamma\text{-Al}_2\text{O}_3\text{-B}$ samples to determine TIE values for dihydrogen dissociative adsorption. Samples (ca. 1 g) were treated at 723 K in flowing H_2 ($1.33 \text{ cm}^3 \text{ g}^{-1} \text{ s}^{-1}$; UHP grade, Praxair; a 0.083 K s^{-1} heating rate) for 1 h and then evacuated for 2 h. After evacuation, samples were brought to the target chemisorption temperature, and H_2 (or D_2) uptakes were measured by increasing the H_2 (or D_2) pressure from 0.1 to 30 kPa (H_2 , Praxair, UHP; D_2 , Spectra Gases Inc., UHP). The apparent cell volume was determined at each temperature using He as a non-adsorbing inert gas.

2.3. Measurement of Isotopic Exchange Rates. Isotopic exchange rates were measured on samples (0.0005–0.0500 g, $<100 \mu\text{m}$ aggregate diameter) held on a quartz frit within a U-shaped quartz tube (6.35 mm O.D., 4 mm I.D.). H_2 (99.999% UHP; Praxair), D_2 (99.8% isotopic purity, Research Grade; Praxair), and N_2 ^a (99.998%, Praxair) streams were treated using purifiers (VICI Metronics) designed to remove residual H_2O and O_2 . Molar flow rates were controlled using electronic mass flow controllers (Parker Porter 200 series). Samples were treated in flowing H_2 ($100 \text{ cm}^3 \text{ g}^{-1} \text{ s}^{-1}$) while heating from ambient temperature to 873 K (at 0.083 K s^{-1}) for $\text{Pt}/\text{SiO}_2\text{-A}$, $\text{Pt}/\gamma\text{-Al}_2\text{O}_3\text{-A}$, and Pt black samples and to 623 K for $\text{Pt}/\text{SiO}_2\text{-B}$ samples and then holding for 2 h before isotopic exchange rate measurements.

The inlet and outlet streams were speciated using mass spectrometry (Leybold Inficon Transpector, TSP TH200). $\text{H}_2\text{-D}_2$ exchange rates were determined by correcting measured rates (r_{n}) for approach to isotopic equilibrium (η) to give forward rates (r_{f}) using

$$r_{\text{n}} = r_{\text{f}}(1 - \eta) \quad (6)$$

The approach to equilibrium (η) for $\text{H}_2\text{-D}_2$ exchange



is defined as

$$\eta = \frac{(\text{HD})^2}{(\text{H}_2)(\text{D}_2)} \frac{1}{K_{\text{HD}}} \quad (8)$$

(i) denotes the pressure of species i (in kPa). K_{HD} is the equilibrium constant for $\text{H}_2\text{-D}_2$ exchange; it equals 4 at all temperatures, corresponding to the binomial isotopologue distribution.⁴³ The thin catalyst beds used in these experiments exhibit hydrodynamics that resemble well-mixed systems; thus, exit concentrations were used in eq 8. The absence of diffusional corruptions of measured exchange rates was confirmed by similar measured exchange rates as the size of the catalyst aggregates was varied (smaller particles, $<50 \mu\text{m}$ aggregate diameter, were obtained by grinding catalyst samples into fine powders; SI-1).

2.4. Computational Methods. Periodic plane wave DFT calculations were performed using the Vienna Ab initio Simulation Package (VASP)^{44,45} as implemented in the computational catalysis interface.⁴⁶ Plane waves were constructed using projector augmented waves^{47–49} with an energy cutoff of 396 eV. (This value errs on the side of greater accuracy and was chosen to facilitate follow-up studies that include $\text{H}_2\text{-D}_2$ exchange in the presence of H_2O .) The revised Perdew–Burke–Ernzerhof (RPBE) form of the generalized gradient approximation (GGA) was used to describe exchange and correlation energies.^{50,51} Wave functions were converged

until the electronic energies varied by less than 10^{-6} eV. Forces on all atoms were determined using a fast Fourier transform grid with a cutoff equal to twice the plane wave cutoff; the geometries of all structures were optimized until the forces on all atoms were smaller than 0.05 eV nm $^{-1}$.

H $_2$ molecules in the gas phase were modeled by placing them within a $1.8 \times 1.8 \times 1.8$ nm vacuum unit cell. Pt(111) surfaces were modeled as 3×3 , 4×4 , and 6×6 closed-packed periodic lattices with four layers orthogonal to the surface and 1 nm of vacuum separating slabs; the bottom two layers were fixed at their bulk positions (an fcc crystal with unit cell parameter of 0.39239 nm),⁵² and the top two layers were relaxed. Sampling of the Brillouin zone depended on the size of the metal surface. For 4×4 Pt(111) surfaces, a $3 \times 3 \times 1$ Monkhorst–pack sampling of the first Brillouin zone (k -point mesh)⁵³ was used during geometric convergence iterations; after convergence, a single-point calculation with a $6 \times 6 \times 1$ k -point mesh was performed to determine electronic energies. These k -point meshes were adjusted to consistently capture long-range interactions for 3×3 Pt(111) surfaces to $4 \times 4 \times 1$ and $8 \times 8 \times 1$ for the geometric convergence and single-point calculation, respectively. For 6×6 Pt(111) surfaces, the meshes were $2 \times 2 \times 1$ and $4 \times 4 \times 1$. Symmetric cubooctahedral Pt nanoparticles (Pt $_{201}$, 201 atoms, a 1.4 nm diameter) with 1.4 nm of vacuum between metal atoms were also examined as model systems, as described in detail in previous reports.^{7,41,54,55} The Brillouin zone was sampled only at the Γ -point for nanoparticle model calculations.

Vibrational frequencies were calculated for bound species and transition states using a fixed displacement method (two displacements per mode), in which all metal atoms were fixed and all H atoms (ranging from 9 to 38 total H atoms) were allowed to vibrate for Pt(111) calculations. For Pt $_{201}$ nanoparticle calculations, only the reacting H $_2$ and H* on the active (111) terrace were allowed to vibrate (19–33 total H atoms). These frequency calculations were used, together with statistical mechanic formalisms and harmonic oscillator models, to estimate vibrational zero-point energies, enthalpies, entropies, and Gibbs free energies. For gaseous H $_2$ molecules, the translational and rotational enthalpies and free energies were also computed instead of using experimental values.

The atomic masses of elements (i.e., using the H or D isomer) have negligible impacts on the potential energies but do impact the enthalpies and free energies of species by altering vibrational frequencies and thus zero-point vibrational energies as well as the vibrational enthalpies and free energies through statistical mechanics formalisms.⁵⁶ For gaseous molecules, atomic masses affect the rotational and translational contributions to free energies; as a result, they influence barriers when transition-state free energies are referenced to gaseous H $_2$ (or D $_2$), as required for comparisons with experimental values in this study. Enthalpy barriers for H $_2$ –D* and D $_2$ –H* reactions can thus be calculated from statistical mechanics by altering atomic weights when calculating vibrational, translational, and rotational partition functions to estimate the kinetic effects of isotopes from free-energy barriers.

3. RESULTS AND DISCUSSION

3.1. Pt Dispersions and Nanoparticle Diameters.

Fractional Pt dispersions were measured for three Pt/SiO $_2$ samples and two Pt/ γ -Al $_2$ O $_3$ samples; these data were used to calculate nanoparticle diameters using eqs 4 and 5 (Table 1).

Table 1. Nominal Metal Contents, Dispersions, and Calculated Particle Diameters

sample	nominal Pt content (% wt)	dispersion	mean nanoparticle diameter (nm) ^b
Pt/SiO $_2$ -A	0.2	0.38	3.2
Pt/SiO $_2$ -B	0.2	1.0	1.5
Pt/SiO $_2$ -C	5.0	0.32	3.8
Pt/ γ -Al $_2$ O $_3$ -A	1.0	0.72	1.9
Pt/ γ -Al $_2$ O $_3$ -B ^a	1.6	0.37	3.3

^aSynthesis and characterization reported in a previous study.³³

^bCalculated by assuming hemispherical particle geometries and using the bulk density of Pt (21.45 g cm $^{-3}$).⁴² H/Pt $_s$ stoichiometries and diameters were estimated using eqs 4 and 5.

3.2. H $_2$ and D $_2$ Uptake on Pt/SiO $_2$ -C and Pt/ γ -Al $_2$ O $_3$ -B and Thermodynamic Isotope Effects. H $_2$ and D $_2$ chemisorption uptake values were measured on 5.0% wt Pt/SiO $_2$ -C and 1.6% wt Pt/ γ -Al $_2$ O $_3$ -B samples at 623 K (10^{-4} to 10^1 kPa). H $_2$ and D $_2$ uptake isotherms (Figure 1) were very

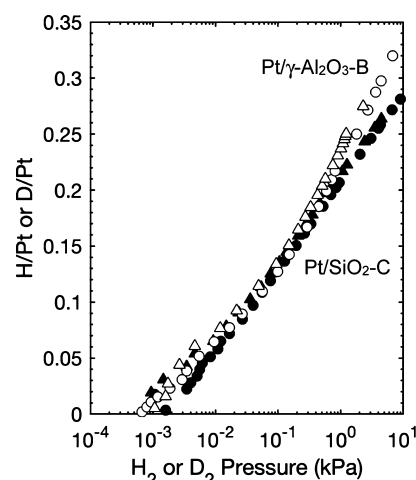


Figure 1. H $_2$ (●, ○) and D $_2$ (▲, △) adsorption isotherms on Pt/SiO $_2$ -C (closed symbols) and Pt/ γ -Al $_2$ O $_3$ -B (open symbols) at 623 K.

similar on each given sample; the uptakes (of both isotopes) differed between Pt/SiO $_2$ -C and Pt/ γ -Al $_2$ O $_3$ -B because of their different metal dispersion (Table 1).³³ These uptake data were used to determine dissociative adsorption equilibrium constants for H $_2$ (K_H) and D $_2$ (K_D)

$$K_H = \frac{\theta_H^2}{(H_2)\theta_s^2} \quad (9)$$

$$K_D = \frac{\theta_D^2}{(D_2)\theta_s^2} \quad (10)$$

θ_H and θ_D are the fractional surface coverages of H* and D* adatoms, respectively, defined as the number of H (or D) atoms adsorbed at a given pressure divided by the number of atoms adsorbed at saturation, and θ_s is fraction of unoccupied sites. The ratio of these adsorption equilibrium constants gives the TIE ($TIE = K_H/K_D$) for dissociative dihydrogen adsorption. These equilibrium constants and TIE ratios are shown as a function of fractional surface coverage in Figure 2. TIE ratios are only slightly influenced by coverage (slopes of 0.13 ± 0.13 and -0.25 ± 0.23 on Pt/SiO $_2$ -C and Pt/ γ -Al $_2$ O $_3$ -B, respectively). These ratios are near unity on Pt/SiO $_2$ -C

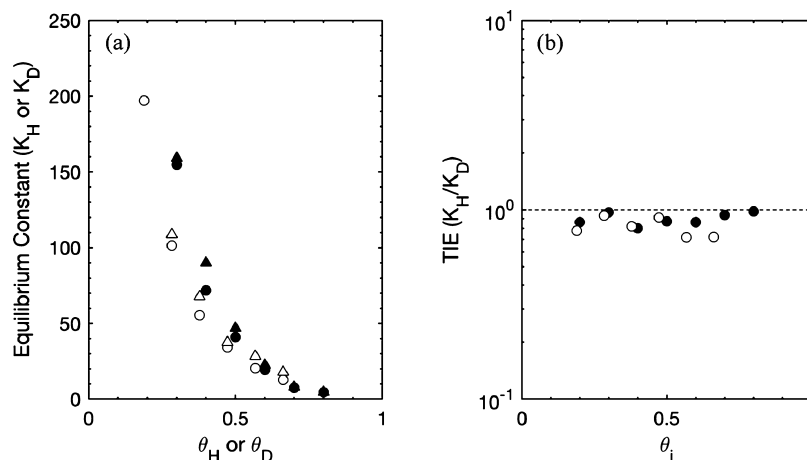


Figure 2. (a) Equilibrium constants for H_2 (K_{H} ; \bullet , \circ) and D_2 (K_{D} ; \blacktriangle , \triangle) dissociative adsorption at different fractional surface coverages on Pt/SiO₂-C (closed symbols) and Pt/ γ -Al₂O₃-B (open symbols). (b) Thermodynamic isotope effects ($\text{TIE} = K_{\text{H}}/K_{\text{D}}$; eqs 9 and 10) at different fractional surface coverages on Pt/SiO₂-C (\bullet) and Pt/ γ -Al₂O₃-B (\circ) at 623 K. The dashed line indicates the position of unity.

(0.90 ± 0.07) and Pt/ γ -Al₂O₃-B (0.81 ± 0.10) at all H_2 and D_2 pressures (10^{-4} to 10^1 kPa) and coverages and agree well with DFT-derived values for Pt(111) surfaces (0.68, 0.87, and 0.91 for atop, fcc, and hcp binding modes, respectively; 1 H/Pt_{surf}, 623 K).⁵⁷

H_2 and D_2 adsorption isotherms were also measured at other temperatures (523–673 K; isotherms and equilibrium constants in SI-2) on 1.6% wt. Pt/ γ -Al₂O₃-B to determine temperature effects on TIE values. Figure 3 shows the average

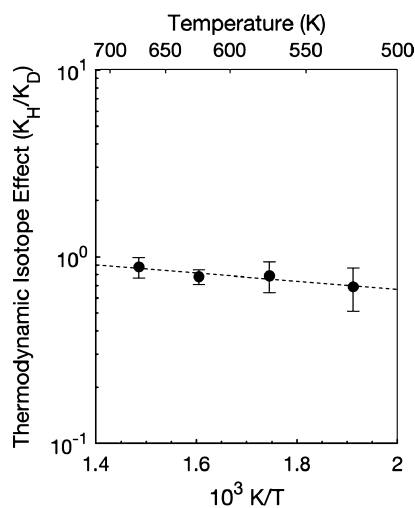


Figure 3. Mean TIE ratios ($\text{TIE} = K_{\text{H}}/K_{\text{D}}$) (averaged across H^* or D^* fractional coverages, 0.19–0.57) at varying temperatures (523–673 K) on Pt/ γ -Al₂O₃-B. The dashed line represents the line of best fit.

TIE values (523–673 K), reflecting the mean over the range of fractional coverages (0.19–0.57) in view of their weak coverage dependence (Figure 2). These values are nearly independent of temperature (Figure 3), within experimental uncertainty, and reflect the small differences in H_2 and D_2 adsorption enthalpies ($\Delta H_{\text{D}_2, \text{ads}} - \Delta H_{\text{H}_2, \text{ads}} = -4.1 \pm 1.4$ kJ mol⁻¹) and entropies ($\Delta S_{\text{D}_2, \text{ads}} - \Delta S_{\text{H}_2, \text{ads}} = 5.0 \pm 2.0$ J mol⁻¹ K⁻¹)

$$\begin{aligned} \text{TIE} &= \frac{K_{\text{H}}}{K_{\text{D}}} \\ &= \exp \left(\left(\frac{\Delta H_{\text{D}_2, \text{ads}} - \Delta H_{\text{H}_2, \text{ads}}}{RT} \right) + \left(\frac{\Delta S_{\text{D}_2, \text{ads}} - \Delta S_{\text{H}_2, \text{ads}}}{R} \right) \right) \end{aligned} \quad (11)$$

Equation 11 can be used to extrapolate TIE values to other temperatures and to infer the relative coverages of H^* and D^* (eqs 9 and 10) under the conditions of isotopic exchange, described in the following section.

3.3. Effects of H_2 and D_2 Pressures on Exchange Rates and Implications for the Identity and Kinetic Relevance of Elementary Steps. H_2 – D_2 isotopic exchange turnover rates were measured at 383 K over a range of H_2 and D_2 pressures (5–80 kPa) on 0.2% wt. Pt/SiO₂-A (3.2 nm, Table 1). The HD formation rates were below detection limits on a Pt-free SiO₂ sample under these conditions. Figure 4 shows

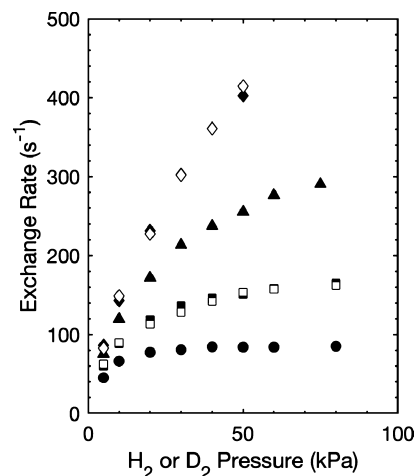


Figure 4. Isotopic exchange rates as a function of H_2 or D_2 pressure at 5 (\bullet), 10 (\blacksquare , \square), 20 (\blacktriangle), and 40 (\blacklozenge , \lozenge) kPa D_2 (closed symbol) or H_2 (open symbol) at 383 K on 0.2% wt. Pt/SiO₂-A. The overlap between closed and open symbols indicates that exchange rates were nearly identical when H_2 and D_2 pressures were switched.

that exchange rates increased monotonically with increasing H₂ or D₂ pressure (5–80 kPa; 0.0625–16 H₂/D₂ molar ratios). HD formation rates were nearly identical when the H₂ and D₂ pressures were switched (as shown by significant overlap between the open and filled symbols of a given type in Figure 4).

These kinetic trends are examined first in the context of the commonly proposed “recombinative desorption” mechanism (eqs 1–3) that such trends, in fact, contradict. HD formation events mediated by recombination of H* and D* (eq 2) depend on the H* and D* coverages set by the thermodynamics of H₂ and D₂ dissociative adsorption and reach maximum values at H₂ and D₂ pressures that lead to identical H* and D* coverages. The chemisorption uptakes reported here (Section 3.2) and in previous studies³³ indicate that Pt surfaces are nearly saturated with H* or D* at all pressures and temperatures used in these exchange experiments [(H₂) + (D₂) > 10 kPa; 383 K]. H* and D* coverages can thus be described by extrapolating TIE ratios from H₂/D₂ chemisorption data on Pt/γ-Al₂O₃-B (523–673 K, Figure 3; Section 3.2) to 383 K, which gives a value of 0.6 ± 0.2. This TIE value (0.6, 383 K) indicates that H* and D* coverages become equal at H₂/D₂ molar ratios of about 1.3, a value estimated by assuming that such TIE values are set by those for desorption rates (derivation in SI-3.1). When TIE values are unity, the rate of HD formation is given by (SI-3.1)

$$r_{\text{HD},f} = k_{-1} \frac{(H_2)(D_2)}{((H_2) + (D_2))^2} \quad (12)$$

and HD formation rates reach a maximum at H₂/D₂ molar ratios of unity. Measured HD formation rates, however, increased monotonically with increasing H₂ and D₂ pressure (Figure 4), even at very high H₂/D₂ molar ratios (16). Such trends are inconsistent with the dissociation–recombination exchange routes depicted by eqs 1–3 and with the rate equation associated with such elementary steps (eq 12). These exchange rate data are also inconsistent with a two-site mechanism, in which H₂ and D₂ molecules adsorb and react in a concerted manner with H*–H*, H*–D*, or D*–D* pairs at surfaces; this latter mechanism would give the rate equation (derivation in SI-3.2, assuming a TIE value of unity)

$$r_{\text{HD},f} = [64k_{-3}(H_2)(D_2)((H_2) + (D_2)) \{ (H_2)^6 + (D_2)^6 + 11(H_2)^2(D_2)^4 + 11(D_2)^2(H_2)^4 - \gamma((H_2)^4 + (D_2)^4 + 4(H_2)^2(D_2)^2) \}] \div [(3(H_2)^2 + (D_2)^2 - \gamma)^2(3(D_2)^2 + (D_2)^2 - \gamma)^2] \quad (13)$$

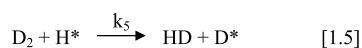
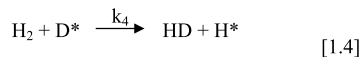
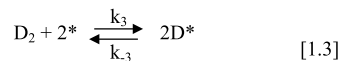
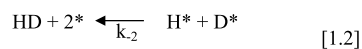
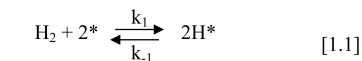
$$\gamma = \sqrt{(H_2)^4 + 14(H_2)^2(D_2)^2 + (D_2)^4} \quad (14)$$

Equations 13 and 14 similarly predict a maximum in HD formation rate at H₂/D₂ molar ratios near unity, in contradiction of the trends in Figure 4. Parity plots of measured and predicted HD formation rates (Figure S4 in SI-4) confirm that these mechanisms are inadequate to describe measured exchange rates.

An alternate exchange pathway is a single-site route in which gaseous H₂ and D₂ molecules react with single D* and H* adatoms to exchange their isotopes, as suggested in previous studies;^{25,27–32} these studies proposed that gaseous H₂ molecules react directly with D* adatoms (or D₂ with H*)

via an “associative” concerted pathway. Such single-site routes may also reflect the adsorption of H₂ and D₂ at non-competitive sites and their subsequent reaction with D* and H*, as shown in the present study from DFT treatments (Section 3.6). These “non-competitive adsorption” exchange pathways are depicted as steps 1.4–1.5 in Scheme 1, together

Scheme 1. Dissociative–Recombinative (1.1–1.3) and Non-Competitive Adsorption (1.4–1.5) Elementary Steps for H₂–D₂ Isotopic Exchange



with the dissociative–recombinative reactions (steps 1.1–1.3). HD formation rates mediated by the elementary steps in Scheme 1 are given by

$$r_{\text{HD},f} = k_{-2}\theta_H\theta_D + k_4(H_2)\theta_D + k_5(D_2)\theta_H \quad (15)$$

Here, θ_i is the fractional coverage of species *i*. Equation 15 contains separate terms for H₂–D* and D₂–H* reactions (steps 1.4–1.5, Scheme 1) to take into account any KIEs ($KIE_{\text{ex}} = k_4/k_5$) for these exchange events. The value of KIE_{ex} can be inferred here from the HD formation rates that are nearly identical when the magnitudes of the H₂ and D₂ pressures are switched (Figure 4, indicated by overlapping open and filled symbols of a given type). We define a parameter γ_{ij} as an inlet stream with H₂ pressure *i* and D₂ pressure *j* (in kPa). Figure 5 shows that the ratios of rates defined as

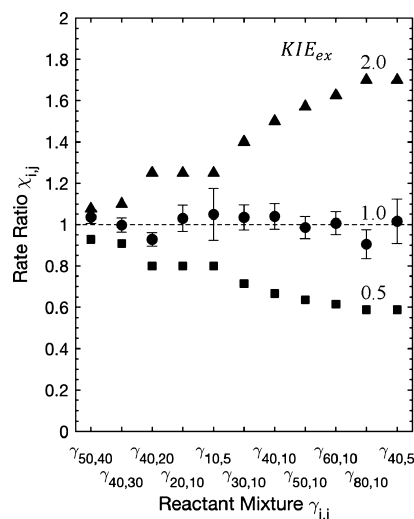


Figure 5. Rate ratios ($X_{i,j} = \frac{r_{\text{HD}}(\gamma_{i,j})}{r_{\text{HD}}(\gamma_{j,i})}$; ●) for reactant mixtures $\gamma_{i,j}$ (H₂ pressure *i* and D₂ pressure *j*). Calculated ratios are included for KIE_{ex} (k_4/k_5) values of 0.5 (■) and 2.0 (▲) for comparison.

$$\chi_{ij} = \frac{r_{\text{HD}}(\gamma_{ij})}{r_{\text{HD}}(\gamma_{ji})} \quad (16)$$

are near unity (1.01 ± 0.05) for all H_2 – D_2 pressure pairs. The χ_{ij} values were also calculated (details in SI-5) using various KIE_{ex} (k_4/k_5) values (0.5–2) that led to significant deviations of χ_{ij} values from unity (0.6–1.7; Figure 5). These experimental values of χ_{ij} (Figure 5) show that KIE_{ex} (k_4/k_5) values are near unity (1.1 ± 0.3), in agreement with values derived later using theoretical methods (Section 3.6). These χ_{ij} values near unity differ from those expected for H^* and D^* coverages derived from the TIE value at 383 K (0.6 ± 0.2). Such deviations suggest that the H_2 – D^* and D_2 – H^* reactions (steps 1.4–1.5, Scheme 1) that mediate the exchange of hydrogen and deuterium atoms occur at rates much faster than dissociation–recombination events (steps 1.1–1.3, Scheme 1). Fractional H^* (θ_{H}) and D^* (θ_{D}) coverages in this case (for a KIE_{ex} value of 1) are, as for a TIE value of unity, described by (derivation in SI-3.3)

$$\theta_{\text{H}} = \frac{(\text{H}_2)}{(\text{H}_2) + (\text{D}_2)} \quad (17)$$

$$\theta_{\text{D}} = \frac{(\text{D}_2)}{(\text{H}_2) + (\text{D}_2)} \quad (18)$$

These H^*/D^* ratios (eqs 17 and 18) are equal to the H_2/D_2 ratios in the contacting gas phase.

Equations 17 and 18 can be substituted into eq 15 to give

$$r_{\text{HD,f}} = k_{-2} \frac{(\text{H}_2)(\text{D}_2)}{((\text{H}_2) + (\text{D}_2))^2} + 2k_4 \frac{(\text{H}_2)(\text{D}_2)}{(\text{H}_2) + (\text{D}_2)} \quad (19)$$

for KIE_{ex} (k_4/k_5) values of unity. This equation includes terms for dissociation–recombination reactions ($k_{-2} \frac{(\text{H}_2)(\text{D}_2)}{((\text{H}_2) + (\text{D}_2))^2}$; steps 1.1–1.3, Scheme 1) and non-competitive-adsorption-mediated exchange reactions ($2k_4 \frac{(\text{H}_2)(\text{D}_2)}{(\text{H}_2) + (\text{D}_2)}$; steps 1.4–1.5, Scheme 1). Equation 19 can also be expressed in a linear form that allows the rate constants k_{-2} and k_4 (normalized per surface site) to be regressed linearly from measured isotopic exchange rates

$$\frac{r_{\text{HD,f}}((\text{H}_2) + (\text{D}_2))^2}{(\text{H}_2)(\text{D}_2)} = k_{-2} + 2k_4((\text{H}_2) + (\text{D}_2)) \quad (20)$$

Figure 6 shows these rates at 383 K according to the functional form of eq 20. The value of k_{-2} ($-2.1 \pm 20 \text{ s}^{-1}$) is given by the y-intercept of the data in Figure 6, while the value of k_4 ($9.1 \pm 0.2 \text{ kPa}^{-1} \text{ s}^{-1}$) is reflected in the slope (uncertainties are defined as 95% confidence intervals). The near-zero value and large uncertainty of k_{-2} show that recombinative hydrogen desorption reactions (steps 1.1–1.3 in Scheme 1) are much slower than H_2 – D^* and D_2 – H^* exchange routes (steps 1.4–1.5 in Scheme 1), as previously suggested by χ_{ij} values near unity (Figure 5); consequently, such dissociative routes contribute negligibly to measured exchange rates under these reaction conditions (383 K, 5–80 kPa H_2 or D_2). A sensitivity analysis of k_{-2} indicates that the rates of recombination are below the detection limit of these experiments (SI-6). A parity plot of the HD formation rates modeled by eq 20 and Scheme 1 is shown as Figure S4c in SI-4.

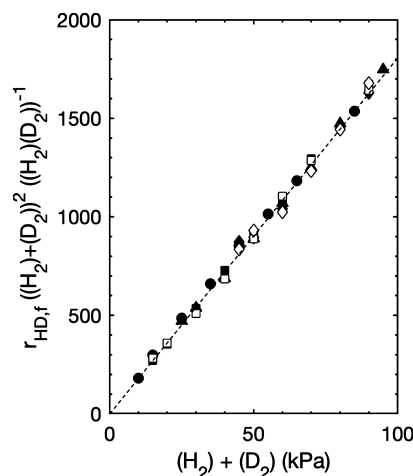


Figure 6. H_2 – D_2 exchange rate data at 5 (●), 10 (■, □), 20 (▲), and 40 (◆, ◇) kPa H_2 (open symbol) or D_2 (closed symbol) at 383 K on 0.2% wt Pt/ SiO_2 -A, linearized in accordance with eq 20. The dashed line represents linear regression of the data.

These data and mechanistic considerations, later probed also by theoretical treatments (Section 3.6), show that H_2 – D_2 exchange occurs on surfaces saturated with a mixture of H^* and D^* adatoms at relative coverages dictated by the reactions of H_2 with D^* and D_2 with H^* (steps 1.4–1.5, Scheme 1) with KIE values near unity; these steps occur much faster than H_2 or D_2 dissociation or H^* – H^* , H^* – D^* , and D^* – D^* recombination reactions (steps 1.1–1.3 in Scheme 1) and lead to H^*/D^* ratios that resemble H_2/D_2 molar ratios in the contacting gas phase. Consequently, the specific value of the TIE for H_2 and D_2 dissociative adsorption does not influence H_2 – D_2 isotopic exchange rates.

3.4. Effects of Temperature and H^*/D^* Coverage on Isotopic Exchange Rates. H_2 – D_2 exchange rates were measured at temperatures between 303 and 1000 K on Pt/ SiO_2 -A at H_2 and D_2 pressures between 2 and 20 kPa. HD formation rates via recombinative desorption routes (step 1.2, Scheme 1) would depend only on the relative ratio of H_2 and D_2 and remain independent of total pressure at each given H_2/D_2 ratio (first term in eq 19), in contrast with H_2 – D^* and D_2 – H^* non-competitive adsorption reactions, which would depend also on the total H_2 and D_2 pressure (through the second term in eq 19). As a result, lower combined H_2/D_2 pressures lead to smaller relative contributions of H_2 – D^* and D_2 – H^* reactions (steps 1.4–1.5, Scheme 1) to measured exchange rates; the contribution from recombination routes (steps 1.1–1.3, Scheme 1) and its rate parameter (k_{-2}) thus become easier to detect at lower total pressures of H_2 and D_2 , as shown by rearranging eq 19 as

$$\frac{r_{\text{HD,f}}((\text{H}_2) + (\text{D}_2))}{(\text{H}_2)(\text{D}_2)} = \frac{k_{-2}}{(\text{H}_2) + (\text{D}_2)} + 2k_4 \quad (21)$$

The value of k_{-2} and its temperature dependence become measurable at sufficiently low combined H_2 and D_2 pressures.

Figure 7 shows $\frac{r_{\text{HD,f}}((\text{H}_2) + (\text{D}_2))}{(\text{H}_2)(\text{D}_2)}$ ratios (left-hand side of eq 21) at several H_2 and D_2 pressures (2–20 kPa) as a function of temperature in an Arrhenius-type plot. These data deviate from linear trends at temperatures above 700 K (Figure 7b); these deviations become more evident at lower combined H_2/D_2 pressures as contributions from dissociation–recombination

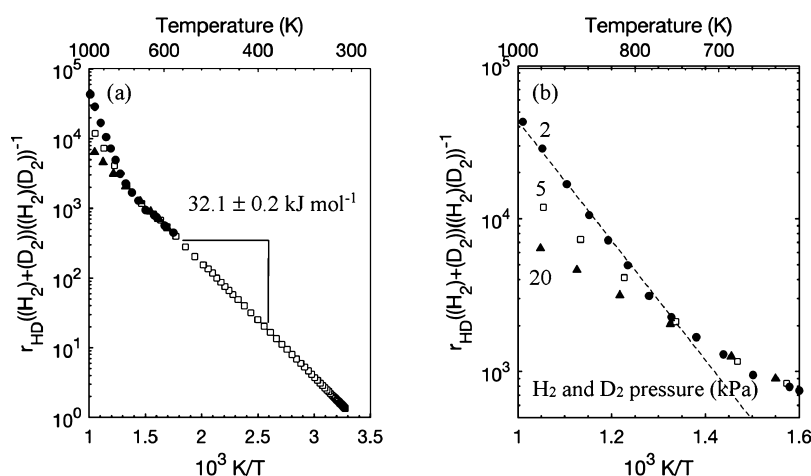


Figure 7. Arrhenius plot of H_2 – D_2 exchange rates on 0.2% wt. Pt/SiO₂-A at 2 kPa H_2 and 2 kPa D_2 (●), 5 kPa H_2 and 5 kPa D_2 (□), and 20 kPa H_2 and 20 kPa D_2 (▲) between (a) 303 and 1000 K and (b) 625 and 1000 K. The dashed line in (b) represents data used to extract the values of k_{-2} .

routes increase ($\frac{k_{-2}}{(\text{H}_2) + (\text{D}_2)}$ term in eq 21). The contributions from the non-competitive adsorption routes ($2k_4$; eq 21) at high temperatures (>700 K) were estimated by extrapolating the data from temperatures at which $\frac{r_{\text{HD},f}((\text{H}_2) + (\text{D}_2))}{(\text{H}_2)(\text{D}_2)}$ values (left-hand side; eq 21) became similar at all $(\text{H}_2) + (\text{D}_2)$ pressures (2–20 kPa, 303–600 K) (Figure 7a); such convergence indicates that these data reflect dominantly contributions from $\text{H}_2 + \text{D}^*$ and $\text{D}_2 + \text{H}^*$ pathways (steps 1.4–1.5, Scheme 1) and its rate parameter (k_4 , eq 21). The k_{-2} values can be obtained using eq 21 by subtracting the contributions from non-competitive adsorption routes ($2k_4$, eq 21; $\text{H}_2 + \text{D}^*$ and $\text{D}_2 + \text{H}^*$, steps 1.4–1.5, Scheme 1) from the total exchange rates measured at high temperatures (750–1000 K, 2 kPa H_2 , 2 kPa D_2 ; Figure 7b, indicated by dashed line). The temperature dependence of the k_{-2} values obtained using these methods of analysis gave a larger activation barrier (78 ± 11 kJ mol^{−1}) than for the low-temperature route and its k_4 rate parameter (32.1 ± 0.2 kJ mol^{−1}). The larger values observed at high temperatures reflect the more prevalent contributions from recombinative desorption routes (reverse of steps 1.1–1.3) and the higher desorption energies as H^*/D^* coverages decrease with increasing temperature.³³

These temperature trends and the similar $\frac{r_{\text{HD},f}((\text{H}_2) + (\text{D}_2))}{(\text{H}_2)(\text{D}_2)}$ values below 700 K (Figure 7a) demonstrate that H_2 – D_2 isotopic exchange at relevant dihydrogen pressures (>5 kPa H_2) occurs almost exclusively via reactions between H_2 and D^* (or D_2 and H^*) (steps 1.4–1.5, Scheme 1); these routes avoid the need to desorb H^* or D^* from equilibrated H^*/D^* adlayers as part of each exchange turnover. Consequently, the reversibility of dissociative dihydrogen adsorption and H^*-H^* (or H^*-D^* , D^*-D^*) recombination (steps 1.1–1.3, Scheme 1) during hydrogenation–dehydrogenation catalysis cannot be determined solely from H_2 – D_2 isotopic exchange rates during catalysis.

3.5. Effect of Catalyst Support and Particle Size on Isotopic Exchange Rates. H_2 – D_2 isotopic exchange rates were measured on 0.2% wt. Pt/SiO₂-A, 0.2% wt. Pt/SiO₂-B, and 1% wt. Pt/ γ -Al₂O₃-A at temperatures between 303 and 433 K in order to examine the effects of the support and Pt nanoparticle diameter (1.5–3.2 nm) on exchange rates and

activation energies. Rates were also measured on unsupported Pt powders (mean diameter of 374 nm). These latter samples sintered significantly during pretreatments at 873 K (Section 2.3), leading to a reduction in surface area available for catalytic turnovers. The small amount of Pt powders (ca. 0.0005 g) used in kinetic studies and the low surface area following such sintering were not amenable to surface area measurements by N₂ adsorption methods; reported rates and mean particle diameters in Pt powder samples were therefore calculated by assuming that the turnover rates on these catalysts were identical to those on Pt/SiO₂-A at 383 K (171 ± 2 s^{−1}; 20 kPa H_2 , 20 kPa D_2). Figure 8 shows $\frac{r_{\text{HD},f}((\text{H}_2) + (\text{D}_2))}{(\text{H}_2)(\text{D}_2)}$

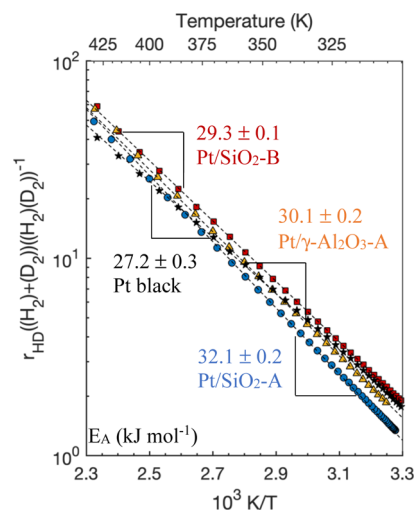


Figure 8. Arrhenius plot of H_2 – D_2 exchange rates and activation energies on (●) 0.2% wt. Pt/SiO₂-A, (■) 0.2% wt. Pt/SiO₂-B, (▲) 1% wt. Pt/ γ -Al₂O₃-A, and (★) Pt black at 20 kPa H_2 and 20 kPa D_2 . Dashed lines represent linear regression of the data.

ratios (left-hand side; eq 21) at different temperatures in an Arrhenius form (20 kPa H_2 , 20 kPa D_2). These temperatures (300–430 K) are much lower than those required for contributions to measured rates from dissociation–recombination routes (steps 1.1–1.3, Scheme 1; Figure 7); as a result, these effects of temperature reflect the activation barrier for k_4 (second term in eq 21; steps 1.4–1.5, Scheme 1). These

activation energies (Table 2) were similar on all samples, consistent with the absence of significant effects of nano-

Table 2. Dispersion, Mean Nanoparticle Diameter, H₂–D₂ Exchange Rate, and Activation Energies of Pt/SiO₂-A, Pt/SiO₂-B, and Pt/γ-Al₂O₃-A^a

catalyst	Pt dispersion	nanoparticle diameter (nm) ^a	H ₂ –D ₂ exchange rate (s ^{−1}) ^b	H ₂ –D ₂ exchange activation energy (kJ mol ^{−1}) ^c
Pt/SiO ₂ -A	0.38	3.2	171 ± 2	32.1 ± 0.2
Pt/SiO ₂ -B	1.0	1.5	183 ± 4	30.1 ± 0.2
Pt/γ-Al ₂ O ₃ -A	0.72	1.9	205 ± 11	29.3 ± 0.1
Pt black	~0.003 ^d	374	171 ^d	27.2 ± 0.3

^aCalculated by assuming hemispherical particle geometries and using the bulk density of Pt (21.45 g cm^{−3}).⁴² H/Pt_s stoichiometries were estimated using eqs 4 and 5. ^bMeasured at 383 K, 20 kPa H₂, and 20 kPa D₂. ^cCalculated for temperatures between 303 and 433 K (20 kPa H₂ and 20 kPa D₂). ^dRates and dispersion of Pt black calculated by assuming negligible particle size effects and equating its exchange activity with that of Pt/SiO₂-A at 383 K.

particle size (1.5–374 nm) on exchange rates (Table 2). These data indicate that the non-competitive adsorption single-site reactions (H₂–D* and D₂–H*; steps 1.4–1.5, Scheme 1) that mediate exchange at 303–433 K and 20 kPa H₂ and 20 kPa D₂ are essentially independent of nanoparticle diameter or the identity of the support (SiO₂, Al₂O₃).

The kinetic dependence of H₂–D₂ isotopic exchange on H₂ and D₂ pressures (5–40 kPa) was also measured on Pt/γ-Al₂O₃-A and Pt black at 383 K, as on Pt/SiO₂-A (Figure 4). HD formation rates on Pt/γ-Al₂O₃-A and Pt black increased monotonically with H₂ and D₂ pressures at all pressures (Figure 9) and, as in the case of Pt/SiO₂-A (Figure 4), were essentially the same when H₂ and D₂ pressures were switched (Figure 9, as indicated by significant overlap between open and closed symbols of the same type). Thus, isotopic exchange rates are well described by eqs 19 and 20 (Figure 10), as in the case of Pt/SiO₂-A (Figure 6; Section 3.2).

The values of k_{-2} and k_4 on Pt/SiO₂-B and Pt black at 383 K are listed in Table 3. The k_{-2} values were essentially 0 on Pt/γ-Al₂O₃-A (−5 ± 40 s^{−1}) and Pt black (−9 ± 49 s^{−1}), as also found on Pt/SiO₂ (−2.1 ± 20 s^{−1}), indicative of negligible contributions from recombinative desorption routes (Scheme

1, steps 1.1–1.3). The value of k_4 on Pt/γ-Al₂O₃-A (10.3 ± 0.6 kPa^{−1} s^{−1}; H₂ or D₂ reactions with D* and H* adatoms; Scheme 1, steps 1.4–1.5) is similar to that measured on Pt/SiO₂-A (9.1 ± 0.2 kPa^{−1} s^{−1}), within experimental uncertainty, consistent with undetectable effects of nanoparticle size (1.9 vs 3.2 nm for Pt/γ-Al₂O₃-A and Pt/SiO₂-A, respectively; Table 2) on exchange turnover rates.^b The near-identical activation energies (Figure 8) and kinetic trends on Pt black and Pt/SiO₂ (Figures 4 and 9) indicate that H₂–D* and D₂–H* exchange events are not mediated (or affected) by any hydrogen-spillover phenomena that could involve migration of H atoms dissociated on Pt nanoparticles to exchange sites on supports.⁵⁸ The similar kinetic trends with H₂ and D₂ pressure on Pt/SiO₂-A, Pt/γ-Al₂O₃-A, and Pt black samples (Figures 4 and 9) are consistent with a similar single-site non-competitive adsorption mechanism, in which H₂ adsorbs and reacts with D* (or D₂ with H*) via steps that are not significantly affected by changes in surface structure induced by varying nanoparticle size or the nature of the support (Table 3).

3.6. Theoretical Treatments of H₂–D₂ Exchange Elementary Steps on Pt Surfaces at Near-Saturation Hydrogen Coverages.

The kinetic trends described above can identify the involvement of specific routes and the absence of others, but they are not able to discern the precise interactions and geometries involved in the formation of the transition states that mediate H₂–D* (and D₂–H*) reactions at the prevalent H* (and D*) coverages. More specifically, the “non-competitive” nature of the H₂ “binding” at the isotopic exchange transition state for H₂ reactions with D* may involve reactions such as (i) a gaseous H₂ molecule; (ii) a physisorbed H₂ molecule interacting weakly with the D* adlayer; or (iii) a H₂ molecule interacting with “spaces” made available within D*(H*) adlayers, but without requiring the prior desorption of a chemisorbed D* atoms. The first two routes are those proposed from measured kinetic data in previous studies.^{25–32} All three routes would lead to rates described by the same rate equation (eq 19, second term) and by the molecularity of the elementary reactions depicted as steps 1.4–1.5 (Scheme 1).

Theoretical methods (DFT) are used to describe the nature of the H* adlayers on Pt surfaces, the interactions among H₂-derived species and these adlayers, and the plausible intermediates and transition states that mediate the exchange of H atoms between a H₂ molecule and a bound H*. H* atoms formed via H₂ dissociation events can bind to atop, bridge, and

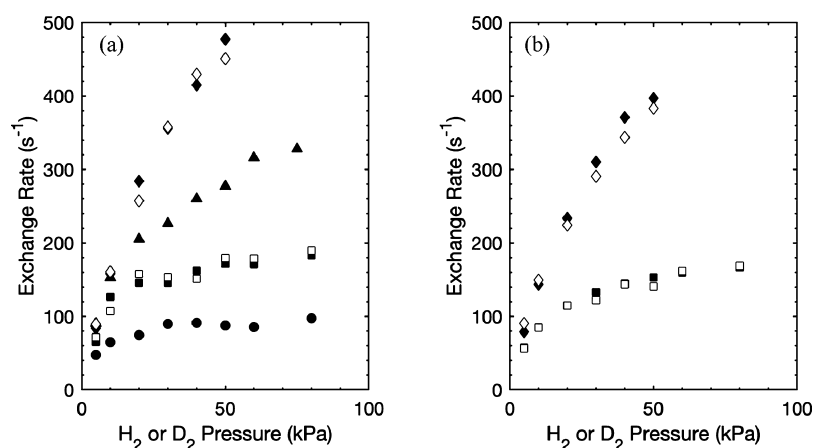


Figure 9. H₂–D₂ exchange rates as a function H₂ or D₂ pressure on (a) 1% wt. Pt/γ-Al₂O₃-A and (b) Pt black at 5 (●), 10 (■, □), 20 (▲), and 40 (◆, ◇) kPa H₂ (open symbol) or D₂ (closed symbol) at 383 K.

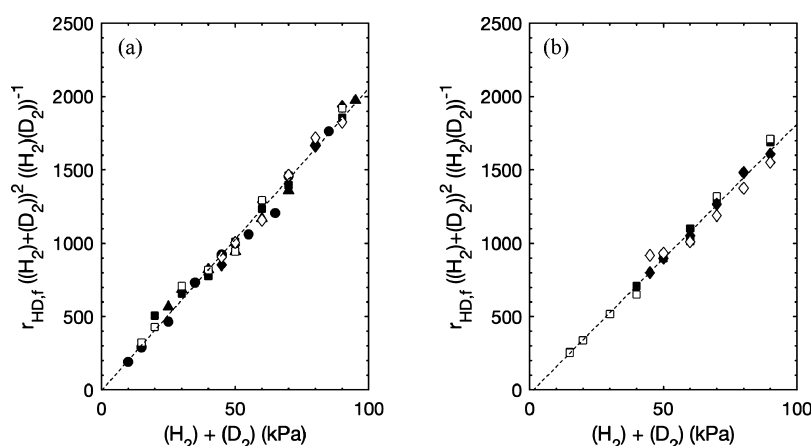


Figure 10. H_2 – D_2 exchange rates linearized in the form of eq 20 on (a) 1% wt. Pt/ γ - Al_2O_3 -A and (b) Pt black at 5 (●), 10 (■, □), 20 (▲), and 40 (◆, ◇) kPa H_2 (open symbol) or D_2 (closed symbol) at 383 K. The dashed line represents the line of best fit of the data.

Table 3. Rate Constants for H_2 – D_2 Exchange on Pt/ SiO_2 -A, Pt/ γ - Al_2O_3 -A, and Pt Black

catalyst	k_{-2} (s^{-1})	k_4 ($\text{kPa}^{-1} \text{s}^{-1}$)
Pt/ SiO_2 -A	-2.1 ± 20	9.1 ± 0.2
Pt/ γ - Al_2O_3 -A	-5 ± 40	10.3 ± 0.6
Pt black	-9 ± 49^a	9.2 ± 0.8^a

^aRates on Pt black calculated by normalizing against Pt/ SiO_2 -A rates at 383 K. The absolute magnitudes of k_{-2} and k_4 on Pt black cannot be compared directly to those on other catalysts.

two distinct (fcc and hcp) threefold sites on Pt(111) surfaces. Atop and threefold sites bind H^* with similar adsorption enthalpies (-18 and -21 kJ mol^{-1} at $1 \text{ H}^*/\text{Pt}_s$). Their small differences in binding energy lie within the inaccuracies of DFT, and the available infrared and thermal desorption data cannot unequivocally discern a preference for one of these binding modes.^{59–61} H_2 – H^* exchange reactions are thus examined on surfaces saturated with H^* atoms ($\text{H}^*/\text{Pt}_s = 1$) present in either atop or fcc binding modes prior to exchange; such exchange reactions can be probed using H_2 – H^* exchange (instead of H_2 – D^*) because theoretical treatments are able to trace individual atoms throughout the reaction coordinate. Calculations of H_2 – D^* and D_2 – H^* reactions on D^* - and H^* -covered surfaces, respectively, were also performed to calculate KIE values. H_2 – H^* exchange reactions were also assessed on 201-atom Pt nanoparticle models (Pt_{201} , 1.8 nm). Such particles exhibit diameters similar to the synthesized samples (Table 1), and the structural model used (flat extended surface vs curved nanoparticle) influences DFT-derived activation barriers for reactions of bound species (e.g., ethane hydrogenolysis on H^* -covered metal particles⁵⁵) and the adsorption enthalpies and saturation coverages for H^* ,⁵⁵ CO^* ,^{54,62–64} NO^* ,^{62,65} and S^* ⁶⁶ on Ru, Rh, Ir, and Pt catalysts. Pt_{201} nanoparticles bind H^* adatoms at atop or fcc sites within their (111) terraces and at a mixture of bridge and atop sites along edges, corners, and (100) terraces; such nanoparticles can achieve H^*/Pt_s ratios larger than unity (SI-7 and previous studies^{41,67–70}). H_2 – H^* exchange reactions were therefore also examined for a range of coverages (1 – $1.8 \text{ H}^*/\text{Pt}_s$) on the Pt(111) terraces of Pt_{201} particles and compared with the results obtained from Pt(111) surface models.

DFT-derived enthalpy and free-energy barriers for H_2 – H^* exchange are used here to assess the relative contributions of the different mechanisms that can account for observed

exchange rates. Measured kinetic effects of H_2 and D_2 pressures on exchange rates (Section 3.3) below 700 K are consistent with these single-site routes (steps 1.4–1.5, Scheme 1) but not with recombinative desorption events as the prevalent route (steps 1.1–1.3, Scheme 1). These single-site routes (steps 1.4–1.5, Scheme 1) involve measured activation barriers of 29 – 32 kJ mol^{-1} (k_4 ; Table 2; range reflects barriers measured on different catalysts) on Pt nanoparticles saturated with H^* and D^* . The elementary steps in Scheme 1 implicate the involvement of a dihydrogen molecule that does not compete for surface sites (*) with the H^* (or D^*) species present at near-saturation coverages and with the reaction of such dihydrogen molecules with H^* (or D^*).

One plausible route for H_2 – H^* reactions involves a metalocycle transition state (TS) (Figure 11a) with a formation enthalpy of 205 kJ mol^{-1} (from $\text{H}_2(\text{g})$ and a H^* on a H^* -covered (atop) Pt(111) surface). This activation barrier is much larger than measured values (29 – 32 kJ mol^{-1} ; Table 2), a consequence of the unstable nature of the H atoms in the metalocycle TS that do not interact with the Pt surface. A dual-site metalocycle-mediated exchange mechanism involving H–H dissociation across a H^* – H^* pair (Figure 11b) gave a barrier of 147 kJ mol^{-1} . This barrier is smaller than that for single-atom metalocycles (210 kJ mol^{-1} , Figure 11a) but remains about 100 kJ mol^{-1} larger than measured values (29 – 32 kJ mol^{-1} , Table 2); this dual-site metalocycle route also predicts kinetic trends (derived in SI-3.2) that contradict the observed effects of H_2 and D_2 pressures on exchange rates. For H^* species bound at fcc sites on Pt(111), no single-site metalocycle transition state could be isolated, and the barrier for the dual-site metalocycle route (140 kJ mol^{-1}) was only slightly smaller than that for H^* at atop sites. These high activation barriers for metalocycle-mediated routes indicate that the H_2 species must interact with the Pt surface in order to exchange one of its H atoms with H^* with barriers resembling those observed experimentally; the measured kinetic trends (described by the second term in eq 19; Section 3.3) dictate that such direct interactions cannot require the intervening desorption of H^* (or D^*) from saturated surfaces.

Such H_2 –Pt interactions and the dissociation of H_2 molecules may be facilitated by displacing H^* adatoms to alternate binding sites (e.g., from atop to fcc) to create “space” for H_2 –Pt interactions at the TS forms. H_2 can thus react in a “sequential” manner, in which H_2 dissociates to form a locally

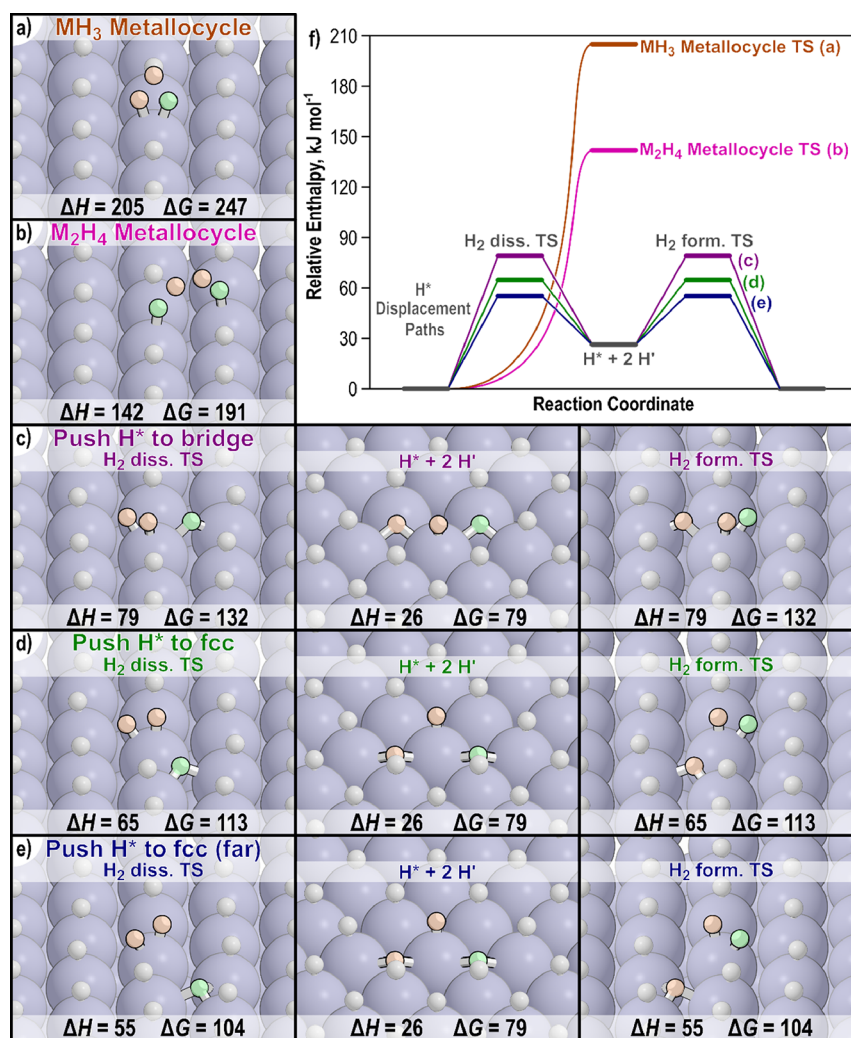


Figure 11. DFT-derived transition-state structures for five H₂ activation routes on Pt(111) surfaces at 1 H*/Pt_s coverages. Hydrogen atoms (typically white) that are highlighted in orange in (a–e) reflect those from gas-phase H₂ and those highlighted in green reflect H* atoms that are reacting directly with H₂ in (a,b) or displaced to adjacent binding modes to accommodate the H₂ dissociation transition state for routes c–e. DFT-derived enthalpies (ΔH) and free energies (ΔG) are shown (at 383 K, 1 bar) relative to a H*-covered surface and H₂(g) for each structure and in the inset reaction coordinate diagram. Reaction mechanisms include those mediated by transition states involving (a) a MH₃ metalloccycle (orange), (b) a M₂H₄ metalloccycle (pink), or the displacement of H* to (c) a vicinal bridge site (purple), (d) a vicinal fcc site (green), and (e) a farther fcc site (blue).

supersaturated H* adlayer, and two nearby H* recombine to form H₂ (shown for H₂–D₂ reactions in Scheme 2). The rate of HD formation from Scheme 2 (derivation in SI-8) is given by

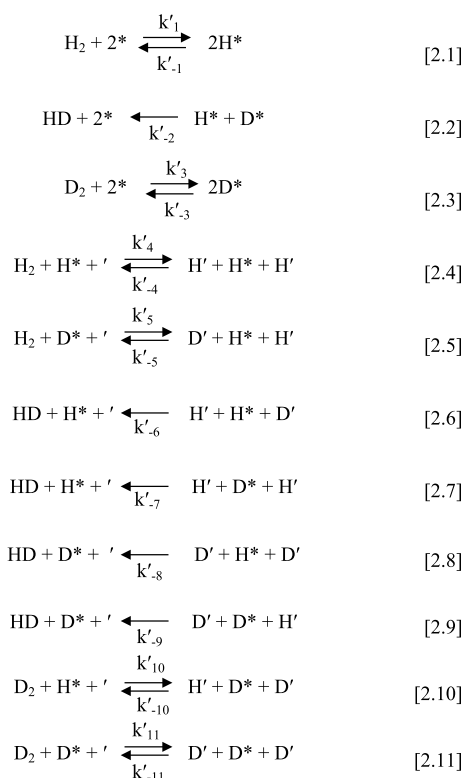
$$r_{\text{HD}} = k'_{-2} \frac{(H_2)(D_2)}{((H_2) + (D_2))^2} + 2k'_4 \frac{(H_2)(D_2)}{(H_2) + (D_2)} \quad (22)$$

Equation 22 was derived by assuming the absence of KIEs (consistent with measured KIE values of 1.1 ± 0.3 , Section 3.3) and that the atop sites (*) are saturated while the fcc sites (') are mostly bare.^c Equation 22 is identical in form to eq 19 and therefore consistent with the exchange rates reported in Section 3.3.

The activation barriers for H₂ dissociation and H*–H' recombination depend on the distance between the displaced H* adatom and the H₂ dissociation transition state. The enthalpy barriers for H₂ dissociation (referenced to a H*(atop)-covered Pt surface; 1 H*/Pt_s) are 79 kJ mol⁻¹ when the H* atom moves from an atop site to a vicinal

bridge site (Figure 11c), 65 kJ mol⁻¹ when H* moves to an adjacent fcc site (Figure 11d), and 55 kJ mol⁻¹ when it moves to an fcc site that is not neighboring the metal site involved in H₂ dissociation (Figure 11e). The enthalpy barriers for H₂–H* exchange on H* adlayers in the fcc binding mode vary from 101 to 116 kJ mol⁻¹ via reactions in which H* atoms shift from fcc to atop sites in order to accommodate the H₂–Pt interactions that stabilize the H₂ dissociation TS (Figure S10 in SI-9). These barriers on fcc-dominated H* adlayers are much larger than those on atop-dominated adlayers. The lowest-enthalpy path involves displacement of H* from atop sites to fcc sites to facilitate H₂ dissociation; however, the activation enthalpies (54–79 kJ mol⁻¹) of this path remain 25–50 kJ mol⁻¹ larger than measured values at low temperatures (<700 K) for Pt/SiO₂-A, Pt/SiO₂-B, and Pt/ γ -Al₂O₃-A (29–32 kJ mol⁻¹, Table 2).

Previous DFT studies of other reactions (e.g., ethane hydrogenolysis on Ir(111) surfaces) at high H* coverages showed that larger-sized surface models (e.g., 6 × 6 instead of

Scheme 2. Proposed Elementary Steps for H₂–D₂ Reactions on Pt Surfaces


4 × 4) led to lower DFT-derived barriers. In this case, the kinetically relevant step for ethane hydrogenolysis has a transition state that is larger than the relevant precursor; decreasing the transition-state density thus reduces through-adlayer repulsions that create periodic artifacts in the barrier calculations.⁵⁵ In the present study, the transition state for dissociating H₂ similarly occupies more surface area than the relevant H*-covered precursor state, which might lead to similar behavior. Therefore, enthalpy barriers were examined for H₂–H* exchange pathways (Scheme 2) on 3 × 3 and 6 × 6 cells on Pt(111) surfaces (Table 4) and compared with the

Table 4. H₂–H* Reaction Enthalpy Barriers, Free-Energy Barriers, and KIE Values on Pt(111) Surfaces of Varying Supercell Sizes (3 × 3, 4 × 4, and 6 × 6) and H* Displacement Locations

supercell size	displaced H* location	enthalpy barrier (kJ mol ⁻¹)	free-energy barrier (kJ mol ⁻¹)	KIE ^a
3 × 3	adjacent fcc	67	114	1.60–1.37
	farther fcc	57	104	1.50–1.25
4 × 4	adjacent bridge	79	132	1.38–1.28
	adjacent fcc	65	113	1.59–1.31
6 × 6	farther fcc	55	104	1.46–1.18
	adjacent fcc	48	90	1.40–1.49
	farther fcc	39	82	1.30–1.35

^aKIE ratios depend on the isotopic identity of spectating H* (or D*) in the adlayer; thus, a range is provided which describes KIE of rate constants for H₂–D* (single D* on H* adlayer) to D₂–H* (single H* on D* adlayer) and for H₂–D* (all D* adlayer) to D₂–H* (all H* adlayer).

results for 4 × 4 cells described above. The enthalpy barrier for H₂–H* exchange decreased from 57 kJ mol⁻¹ on 3 × 3 surfaces to 55 kJ mol⁻¹ on 4 × 4 surfaces and 39 kJ mol⁻¹ on 6 × 6 surfaces when displacing H* to a farther fcc site (Figure 11e for a 4 × 4 surface, Table 4), bringing DFT-derived barriers much closer to measured values (29–32 kJ mol⁻¹; Table 4).

These trends in DFT-derived barriers with cell size (Table 4) reflect the inability of flat periodic surfaces to accommodate disruptions within their adlayer as previously described for other reactions and adsorbates,^{54,55,62–66} this suggests that H₂–H* reactions on non-periodic Pt particle models may represent a more faithful description of experimental systems at near-saturation coverages. H* adatoms bind to atop or fcc sites (Figures S7–S9 in SI-7) on low-index (111) facets of Pt₂₀₁ nanoparticles with similar adsorption energies for the two adlayers over a range of coverages (1.4–1.7 H*/Pt_s), as in the case of Pt(111) surfaces (at 1 H*/Pt_s). On corners, edges, and (100) facets, H* binds in a mixture of bridge and atop modes that depends on H* coverage. Measured H₂–D₂ exchange rates were insensitive to the size of Pt nanoparticles (Table 2), which changes the mean coordination of exposed Pt atoms; these observations indicate that exchange reactions do not occur preferentially at the corner and edge Pt atoms that become more prevalent on smaller nanoparticles. H₂–H* exchange steps were examined H*-covered (111) terraces on Pt₂₀₁, which provides a direct comparison to Pt(111) surface models, with H* atoms located in atop or fcc binding modes and at different total H* coverages (1.15–1.93 H*/Pt_s); suprastoichiometric coverages (>1.0 H*/Pt_s) were achieved by varying the number of H* bound to the corner and edge Pt atoms at the boundaries of the (111) terraces. The enthalpy barrier for H₂ dissociation is 35 kJ mol⁻¹ at 1.15 H*/Pt_s when displacing H* to a nearby (but not adjacent) fcc site (Figure 12b), a value that is similar to that obtained for 6 × 6 cells on Pt(111) surfaces (39 kJ mol⁻¹). Differential adsorption energies of H* increase with increasing H* coverage but remain negative at coverages as high as 1.44 H*/Pt_s and become positive at H*/Pt_s ratios greater than 1.7 H*/Pt_s. This suggests that small Pt particles saturate at coverages above 1.0 H*/Pt_s (SI-7), as shown previously.⁴¹ At the expected coverage of 1.44 H*/Pt_s based on differential adsorption enthalpies (SI-7), the barriers are 27 kJ mol⁻¹, very close to the measured values (29–32 kJ mol⁻¹, Table 2). The H₂–H* exchange activation barriers range from 27 to 58 kJ mol⁻¹ for different coverages within H* adlayers (at 1.15–1.93 H*/Pt_s) that have H* bound at atop sites within their (111) terraces (Figure 12a). Higher barriers (57 and 50 kJ mol⁻¹) at coverages of 1.74 and 1.93 H*/Pt_s are likely irrelevant to experimental conditions because such coverages are unlikely to be present based on the differential adsorption energies (SI-7). Larger barriers were measured at temperatures greater than 700 K; these barriers may reflect the recombinative pathway (steps 1.1–1.3; Scheme 1) and the increase in the enthalpy of desorption with decreasing H* (or D*) coverage as the temperature increases.³³ DFT-based comparisons of the H*-displacement (Scheme 2) and recombinative pathways, however, give inaccurate results because of the large errors in DFT-derived entropies for H*, as shown in earlier studies.³³

The barriers for H*-displacement mechanisms on (111) terraces of Pt₂₀₁ particles that have fcc-bound H* are larger than those with atop-bound H*, with barriers of 74–87 kJ mol⁻¹ for H₂–H* exchange at 1.38–1.67 H*/Pt_s by displacing

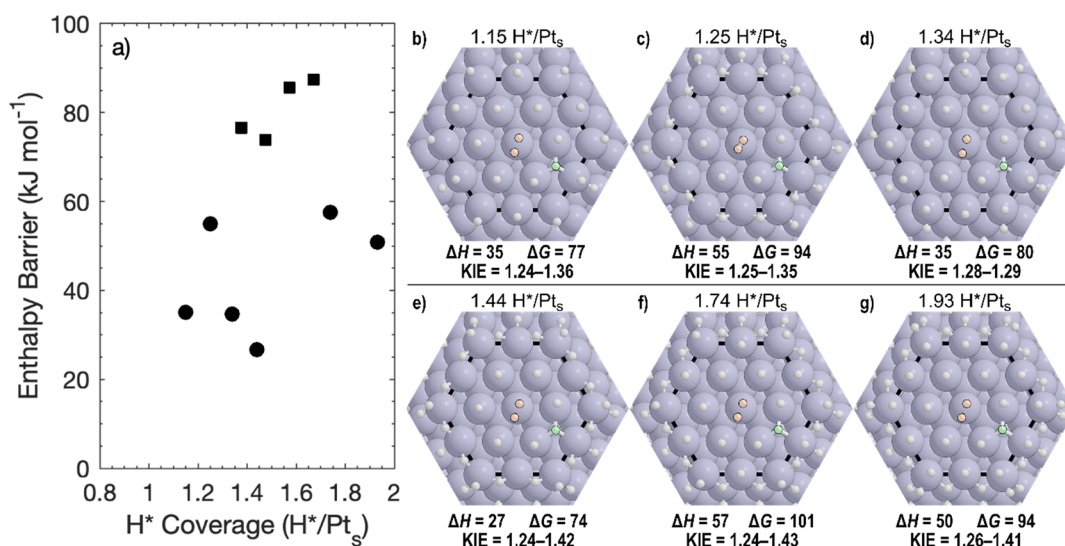


Figure 12. (a) DFT-calculated reaction enthalpy barriers (relative to H₂ in the gas phase and a H*-covered surface) for H₂–H* reactions on Pt₂₀₁ particles (at varying H* coverages) (●) when displacing H* from a top site to a farther fcc site [atop-dominant surfaces, (b–e)] and on Pt₂₀₁ particles (■) when displacing H* from an fcc site to a top site (fcc-dominant surfaces, SI-7). Atoms highlighted in orange reflect those from gas-phase H₂ and those highlighted in green reflect H* atoms displaced to adjacent binding modes to accommodate the H₂ dissociation transition states. KIE values reflect the differences in rate constants for H₂–D* and D₂–H* reactions; ranges reflect changing the isotopic composition of the spectating adlayer.

an fcc H* to an atop H* site to make room on the catalyst surface for H₂ dissociation (Figure S11 in SI-9). These trends demonstrate that fcc-dominant H* adlayers are less reactive than atop-based H* adlayers for H₂–H* exchange and that both atop and fcc adlayers on Pt₂₀₁ nanoparticle models avoid the steric hindrance to lateral relaxation imposed by small (3 × 3, 4 × 4) periodic Pt(111) models as H* is displaced to an alternate binding site in order to accommodate the H₂ dissociation TS.

Experimental KIE values ($k_4/k_5 = 1.1 \pm 0.3$; Scheme 1) were calculated from kinetic data by comparing rate ratios (χ_{ij} ; eq 16; Figure 5, Section 3.3). For instance, the HD formation rates at 40 kPa H₂ and 5 kPa D₂ and at 5 kPa D₂ and 40 kPa H₂ led to a rate ratio of 1.01 ± 0.11 (Figure 5). Such ratios near unity when H₂/D₂ molar ratios were inverted were used to infer that HD formation pathways have KIE values near unity (Section 3.3). Scheme 2, however, shows that HD can form via several pathways (steps 2.6–2.9), each plausibly exhibiting different rate constants. Measurements reflect the appropriate ensemble average over all possible routes forming HD (steps 2.6–2.9; Scheme 2) and all steps that determine the coverages of H*, D*, H', and D' (steps 2.4–2.11; Scheme 2). DFT methods are able to assess KIEs for each step; these require, however, a large number of calculations for all binding locations and combinations of isotopes. As a result, KIE values are estimated for only two representative exchange reactions (H₂–D* and D₂–H*; steps 2.5 and 2.10), which are also included in Scheme 1 (steps 1.4–1.5); these KIE values (k'_5/k'_{10} , Scheme 2; k_4/k_5 , Scheme 1) were obtained by calculating the free-energy barriers for H₂–D* and D₂–H* reactions on Pt(111) surfaces and Pt₂₀₁ catalyst models while varying H*/D* ratios in the rest of the adlayer (consisting of spectating H* or D* atoms).

The free-energy barriers for H₂–D* reactions where D* is displaced to a “farther” fcc site (Figure 11e) vary from 104.8 kJ mol⁻¹ to 105.1 kJ mol⁻¹ on a 3 × 3 Pt(111) surface as the isotopic contents of the spectating adlayer vary from only H*

to only D*. The barriers for D₂–H* reactions vary from 105.8 to 106.1 kJ mol⁻¹ for the same isotopic content range in the spectating adlayer. These data lead to differences in free-energy barrier (ΔΔG) values between these two exchange reactions of ~1 kJ mol⁻¹, favoring H₂–D* exchange; they lead to KIE values (k'_5/k'_{10} , Scheme 2; k_4/k_5 , Scheme 1) of 1.4 for all adlayer isotopic contents. Experimental KIE values, however, were estimated by measuring rates under inverse pressure conditions (Figure 5); thus, k'_5/k'_{10} (Scheme 2) and k_4/k_5 (Scheme 1) were also calculated by comparing free energies for H₂–D* and D₂–H* reactions while also swapping the isotopic content of the spectating adlayer. Using this approach, the k'_5/k'_{10} (Scheme 2) and k_4/k_5 (Scheme 1) values range from 1.50 when comparing H₂–D* (with D* in all spectating positions) and D₂–H* (with H* in all spectating positions) to 1.25 when comparing H₂–D* (with H* in all spectating positions) and D₂–H* (with D* in all spectating positions). These KIE values from 1.25 to 1.50 lie within the experimental uncertainty (1.1 ± 0.3 ; Section 3.3). This same exchange mechanism (Figure 11e) was examined on larger 4 × 4 and 6 × 6 cells on Pt(111) surfaces. The KIE values on these larger periodic cells are typically closer to unity than for 3 × 3 cells; they give KIE ranges of 1.18–1.46 for 4 × 4 and 1.30–1.35 for 6 × 6 surfaces, where the ranges reflect different isotopic compositions within the spectating adlayer. DFT-derived KIE values for H₂–D* and D₂–H* steps on Pt₂₀₁ nanoparticle surfaces were essentially independent of H* and D* combined coverages (1.15–1.93 H*/Pt_s; 1.25–1.43 KIE values). These KIE ranges are consistent with measured values (1.1 ± 0.3 , Section 3.3).

DFT methods indicate that H₂–D₂ exchange occurs predominantly via non-competitive adsorption routes at the temperatures of the kinetic measurements (300–700 K; Section 3.3) in which H₂ (or D₂) displaces D* (or H*) atoms to create spatial access to the Pt surface atoms for dissociation events. Such pathways do not require the intervening removal of D* (or H*) from equilibrated adlayers via recombinative desorption but lead instead to the temporary

local supersaturation of the Pt surface and to a decrease in the H^*/D^* binding energy at such locations;³³ H^*-D' (or D^*-H') recombine to form $HD(g)$, thus completing an exchange turnover. The non-competitive adsorption of H_2 (and D_2) through adatom displacements disrupts the H^*/D^* adlayer in a manner that allows H_2-D_2 exchange to occur at much faster rates than expected from recombinative desorption from equilibrated adlayers, from which recombinative desorption occurs with higher barriers (78 ± 11 kJ mol⁻¹; Section 3.4) than from locally supersaturated surfaces ($39-57$ kJ mol⁻¹; Table 4). Activation enthalpies decrease as the surface model includes a larger number of Pt atoms for periodic Pt(111) surfaces. Such trends indicate that the exchange TS creates adlayer strain through interactions among TS structures in adjacent cells. Nanoparticle models lack such artifacts of periodic systems, thus leading to lower activation enthalpies at H^* coverages of 1.15, 1.34, and 1.44 H^*/Pt_s ; other H^* coverages (1.25, 1.74, 1.93 H^*/Pt_s) give high enthalpy barriers, indicating that activation enthalpies are sensitive to the specific number and arrangement of H^* on the corner and edge atoms that surround the (111) terraces. Periodic and nanoparticle surface models show that H^* adlayers with H^* in atop binding modes on (111) surfaces (or terraces) give smaller exchange barriers than adlayers in which H^* binds at fcc sites, giving better agreement between the former atop-dominated adlayers and the measured kinetic behavior. Activation free energies that determine KIE are essentially independent of the spectating adlayer isotopic content and are also nearly the same for H_2-D^* or D_2-H^* exchange events, leading to DFT-derived KIE values near unity (near 1.3), consistent with experimental results.

4. CONCLUSIONS

H_2-D_2 exchange reactions are frequently employed in mechanistic studies to probe the reversibility of H_2 dissociative adsorption reactions without proper considerations for the thermodynamics of H_2 versus D_2 adsorption or the mechanism by which isotopic exchange events occur. In this study, uptakes of H_2 and D_2 were measured on several Pt-based catalysts to determine TIE values at temperatures (523–673 K) relevant for catalytic hydrogenation/dehydrogenation reactions. These TIE values were near unity and depended only weakly on the temperature of adsorption, corresponding with a 4 kJ mol⁻¹ difference in the dissociative adsorption enthalpy for H_2 and D_2 . Such temperature dependences were used to calculate H^* and D^* equilibrium coverages at the temperatures of H_2-D_2 exchange kinetic studies. These coverages and the kinetic dependences of exchange on H_2 and D_2 pressures at 373 K were shown to be inconsistent with the commonly proposed recombinative desorption pathway. H_2-D_2 exchange reactions instead occur predominantly via single-site reactions between H_2 and D^* (or D_2 and H^*) for temperatures below 700 K. Isotopic exchange rates were also nearly identical when H_2 and D_2 pressures were swapped, reflecting the absence of a KIE and an adlayer whose composition is determined by H_2-D^* or D_2-H^* exchange reactions rather than the thermodynamics (and TIE) of H_2 and D_2 dissociative adsorption. Theoretical calculations showed that these exchange reactions are mediated instead by the non-competitive adsorption and dissociation of H_2 or D_2 onto Pt surfaces at spaces created from the displacement (but not desorption) of H^* and D^* adatoms to alternate binding modes. Activation enthalpies decreased in these calculations as the catalyst model became

larger for Pt(111) surfaces and were lower on Pt nanoparticle models than on periodic surface models, indicating that these exchange transition states cause adlayer strain via through-adlayer interactions in neighboring unit cells within the periodic models. Calculated activation enthalpy barriers and KIE values on the largest surface (6×6 Pt(111)) models and on nanoparticle models were in close agreement with experimental values. The results from this study thus demonstrate that H_2-D_2 isotopic exchange are mediated by reaction pathways that bypass dissociation–recombination reactions at low temperature and therefore cannot be used to conclusively demonstrate the reversibility of H_2 dissociative adsorption reactions on catalytic surfaces.

■ ASSOCIATED CONTENT

Supporting Information

The Supporting Information is available free of charge at <https://pubs.acs.org/doi/10.1021/acs.jpcc.1c09131>.

Effect of catalyst pellet size on reaction rates; H_2 and D_2 chemisorption isotherms on Pt/ γ - Al_2O_3 -B at 523–673 K; derivation of rate equations for H_2-D_2 exchange mechanisms; parity plots of H_2-D_2 exchange models; calculation of exchange rates simulating various magnitudes of KIEs for H_2-D_2 exchange; sensitivity analysis of rate parameters k_{-2} and k_4 ; DFT-derived hydrogen adsorption enthalpies as a function of coverage on Pt(111) surfaces and Pt₂₀₁ particles; derivation of rate equations for DFT-derived H_2-D_2 exchange mechanism; and DFT-derived transition states and enthalpy barriers for H_2-H^* reactions in $H^*(fcc)$ -dominated adlayers on Pt(111) surfaces and Pt₂₀₁ particles (PDF)

■ AUTHOR INFORMATION

Corresponding Author

Enrique Iglesia – Department of Chemical Engineering, University of California at Berkeley, Berkeley, California 94720, United States; orcid.org/0000-0003-4109-1001; Phone: (510) 642-9673; Email: iglesia@cchem.berkeley.edu; Fax: (510) 642-4778

Authors

Samuel L. Leung – Department of Chemical Engineering, University of California at Berkeley, Berkeley, California 94720, United States; orcid.org/0000-0002-0915-1361

David Hibbitts – Department of Chemical Engineering, University of Florida, Gainesville, Florida 32611, United States; orcid.org/0000-0001-8606-7000

Mónica García-Diéguez – Department of Chemical Engineering, University of California at Berkeley, Berkeley, California 94720, United States; Present Address: Johnson Matthey, Billingham, TS23 1LB, United Kingdom

Complete contact information is available at: <https://pubs.acs.org/doi/10.1021/acs.jpcc.1c09131>

Notes

The authors declare no competing financial interest.

■ ACKNOWLEDGMENTS

This study was funded by Chevron Corporation. S.L.L. acknowledges funding from a Chevron Graduate Student Research Fellowship. We also thank Dr. Aaron Sattler for helpful technical discussions.

■ ADDITIONAL NOTES

^aN₂ is used as the inert carrier and internal standard in place of He to avoid overlap with the D₂ 4 amu signal in the mass spectra.

^bAbsolute exchange rates and the value of *k*₄ on Pt black cannot be compared directly because the rates on Pt black were normalized by the rates on Pt/SiO₂-A at 383 K.

^cThe same functional form arises if the choices of the binding modes are switched.

■ REFERENCES

- (1) Atkins, P. W.; De Paula, J. *Atkins' Physical Chemistry*, 9th ed.; Oxford University Press: Oxford; New York, 2010.
- (2) Bigeleisen, J.; Mayer, M. G. Calculation of Equilibrium Constants for Isotopic Exchange Reactions. *J. Chem. Phys.* **1947**, *15*, 261–267.
- (3) Bigeleisen, J.; Wolfsberg, M. Theoretical and Experimental Aspects of Isotope Effects in Chemical Kinetics; *Advances in Chemical Physics*; Wiley Online Library, 1958; Vol. 1, pp 15–76. DOI: 10.1002/9780470143476.ch2
- (4) Melander, L. C. S.; Saunders, W. H. *Reaction Rates of Isotopic Molecules*; Wiley: New York, 1980.
- (5) González-Lafont, À.; Lluch, J. M. Kinetic Isotope Effects in Chemical and Biochemical Reactions: Physical Basis and Theoretical Methods of Calculation. *Wiley Interdiscip. Rev.: Comput. Mol. Sci.* **2016**, *6*, 584–603.
- (6) Sattler, A. Hydrogen/Deuterium (H/D) Exchange Catalysis in Alkanes. *ACS Catal.* **2018**, *8*, 2296–2312.
- (7) Loveless, B. T.; Buda, C.; Neurock, M.; Iglesia, E. Co Chemisorption and Dissociation at High Coverages During Co Hydrogenation on Ru Catalysts. *J. Am. Chem. Soc.* **2013**, *135*, 6107–6121.
- (8) Panpranot, J.; Goodwin, J. G., Jr.; Sayari, A. Effect of H-2 Partial Pressure on Surface Reaction Parameters During Co Hydrogenation on Ru-Promoted Silica-Supported Co Catalysts. *J. Catal.* **2003**, *213*, 78–85.
- (9) Gnanamani, M. K.; Jacobs, G.; Shafer, W. D.; Sparks, D.; Davis, B. H. Fischer-Tropsch Synthesis: Deuterium Kinetic Isotope Study for Hydrogenation of Carbon Oxides over Cobalt and Iron Catalysts. *Catal. Lett.* **2011**, *141*, 1420–1428.
- (10) Yang, J.; Tveten, E. Z.; Chen, D.; Holmen, A. Understanding the Effect of Cobalt Particle Size on Fischer-Tropsch Synthesis: Surface Species and Mechanistic Studies by Ssitka and Kinetic Isotope Effect. *Langmuir* **2010**, *26*, 16558–16567.
- (11) Burwell, R. L. Deuterium as a Tracer in Reactions of Hydrocarbons on Metallic Catalysts. *Acc. Chem. Res.* **1969**, *2*, 289–296.
- (12) Siegel, S.; Ohrt, D. W. Kinetic Hydrogen Isotope Effects in Catalytic Hydrogenation of Alkenes. *J. Chem. Soc. D* **1971**, 1529–1530.
- (13) Osborn, J. A.; Jardine, F. H.; Young, J. F.; Wilkinson, G. Preparation and Properties of Tris(Triphenylphosphine)-Halogenorhodium(I) and Some Reactions Thereof Including Catalytic Homogeneous Hydrogenation of Olefins and Acetylenes and Their Derivatives. *J. Chem. Soc. A* **1966**, 1711–1732.
- (14) Montelatici, S.; van der Ent, A.; Osborn, J. A.; Wilkinson, G. Further Studies on Homogeneous Hydrogenation of Olefins by Use of Tris (Tertiary Phosphine)Chlororhodium(I) Complexes. *J. Chem. Soc. A* **1968**, 1054–1058.
- (15) Jones, W. D.; Feher, F. J. Isotope Effects in Arene C-H Bond Activation by [(C₅Me₅)Rh(Pme₃)]. *J. Am. Chem. Soc.* **1986**, *108*, 4814–4819.
- (16) Jones, W. D. Isotope Effects in C-H Bond Activation Reactions by Transition Metals. *Acc. Chem. Res.* **2003**, *36*, 140–146.
- (17) Logan, S.; Philp, J. Kinetic isotope effects in the catalytic synthesis of ammonia. *J. Catal.* **1968**, *11*, 1–6.
- (18) Ozaki, A. *Isotopic Studies of Heterogeneous Catalysis*; Kodansha, 1977.
- (19) Emmett, P. H. The Use of Isotopic Tracers in Studying Catalysts and Catalytic Reactions. *Catal. Rev.* **1972**, *7*, 1–24.
- (20) Burwell, R. L. The Uses of Deuterium in the Study of Heterogeneous Catalysis. *Catal. Rev.* **1972**, *7*, 25–49.
- (21) Yao, R.; Herrera, J. E.; Chen, L.; Chin, Y.-H. C. Generalized Mechanistic Framework for Ethane Dehydrogenation and Oxidative Dehydrogenation on Molybdenum Oxide Catalysts. *ACS Catal.* **2020**, *10*, 6952–6968.
- (22) Biscardi, J. A.; Iglesia, E. Reaction Pathways and Rate-Determining Steps in Reactions of Alkanes on H-Zsm5 and Zn/H-Zsm5 Catalysts. *J. Catal.* **1999**, *182*, 117–128.
- (23) Cant, N.; Tonner, S. P.; Trimm, D. L.; Wainwright, M. S. Isotopic Labeling Studies of the Mechanism of Dehydrogenation of Methanol to Methyl Formate over Copper-Based Catalysts. *J. Catal.* **1985**, *91*, 197–207.
- (24) Joshi, R.; Zhang, G.; Miller, J. T.; Gounder, R. Evidence for the Coordination-Insertion Mechanism of Ethene Dimerization at Nickel Cations Exchanged onto Beta Molecular Sieves. *ACS Catal.* **2018**, *8*, 11407–11422.
- (25) Breakspere, R.; Norton, P. R.; Eley, D. D. Hydrogen Chemisorption and Exchange on Platinum. *J. Catal.* **1972**, *27*, 215–221.
- (26) Christmann, K.; Ertl, G.; Pignet, T. Adsorption of Hydrogen on a Pt(111) Surface. *Surf. Sci.* **1976**, *54*, 365–392.
- (27) Wachs, I. E.; Madix, R. J. On the H₂-D₂ Exchange on Stepped Platinum Surfaces. *Surf. Sci.* **1976**, *58*, 590–596.
- (28) Gillespie, R. D.; Burwell, R. L.; Marks, T. J. Isotopic Exchange between H₂ and D₂ by the Rideal-Eley Mechanism. *Catal. Lett.* **1991**, *9*, 363–368.
- (29) O'Brien, C. P.; Miller, J. B.; Morreale, B. D.; Gellman, A. J. The Kinetics of H-2-D-2 Exchange over Pd, Cu, and Pdcu Surfaces. *J. Phys. Chem. C* **2011**, *115*, 24221–24230.
- (30) Rideal, E. K. On the Hydrogen-Deuterium Exchange Reaction. *J. Res. Inst. Catal., Hokkaido Univ.* **1968**, *16*, 45–51.
- (31) Eley, D. D.; Norton, P. R. Conversion and Equilibration Rates of Hydrogen on Nickel. *Discuss. Faraday Soc.* **1966**, *41*, 135–148.
- (32) Iida, I. Mechanism of Catalyzed Hydrogen-Deuterium Exchange on Gold Deposited over Poly(Tetrafluoroethylene). *Bull. Chem. Soc. Jpn.* **1979**, *52*, 2858–2862.
- (33) García-Diéguez, M.; Hibbitts, D. D.; Iglesia, E. Hydrogen Chemisorption Isotherms on Platinum Particles at Catalytic Temperatures: Langmuir and Two-Dimensional Gas Models Revisited. *J. Phys. Chem. C* **2019**, *123*, 8447–8462.
- (34) Yang, G.; Akhade, S. A.; Chen, X.; Liu, Y.; Lee, M. S.; Glezakou, V. A.; Rousseau, R.; Lercher, J. A. The Nature of Hydrogen Adsorption on Platinum in the Aqueous Phase. *Angew. Chem., Int. Ed.* **2019**, *58*, 3527–3532.
- (35) Vincent, J. K.; Olsen, R. A.; Kroes, G. J.; Baerends, E. J. Dissociative Chemisorption of H-2 on Pt(111): Isotope Effect and Effects of the Rotational Distribution and Energy Dispersion. *Surf. Sci.* **2004**, *573*, 433–445.
- (36) Nieuwenhuys, B. E. Influence of Surface-Structure on Adsorption of Hydrogen on Platinum, as Studied by Field-Emission Probe-Hole Microscopy. *Surf. Sci.* **1976**, *59*, 430–446.
- (37) Gómez, R.; Orts, J. M.; Álvarez-Ruiz, B.; Feliu, J. M. Effect of Temperature on Hydrogen Adsorption on Pt(111), Pt(110), and Pt(100) Electrodes in 0.1 M HClO₄. *J. Phys. Chem. B* **2004**, *108*, 228–238.
- (38) Poelsema, B.; Lenz, K.; Comsa, G. The Dissociative Adsorption of Hydrogen on Defect-Free Pt(111). *J. Phys.: Condens. Matter* **2010**, *22*, 304006.
- (39) Rootsart, W.; Vanreijen, L. L.; Sachtler, W. M. H. Field-Emission Study of Composite Adsorption Layers on Tungsten and Platinum. *J. Catal.* **1962**, *1*, 416–431.
- (40) de Jong, K. P. *Synthesis of Solid Catalysts*; Wiley-VCH: Weinheim, 2009.

- (41) Almithn, A. S.; Hibbitts, D. D. Supra-Monolayer Coverages on Small Metal Clusters and Their Effects on H-2 Chemisorption Particle Size Estimates. *AIChE J.* **2018**, *64*, 3109–3120.
- (42) Bergeret, G.; Gallezot, P.; Particle Size and Dispersion Measurements. In *Handbook of Heterogeneous Catalysis*; Ertl, G., Knözinger, H., Schüth, F., Weitkamp, J., Eds.; Wiley, 2008; pp 738–765.
- (43) Hanson, R. M.; Green, S. M. E. *Introduction to Molecular Thermodynamics*; University Science Books: Sausalito, Calif., 2008.
- (44) Kresse, G.; Furthmüller, J. Efficient Iterative Schemes for Ab Initio Total-Energy Calculations Using a Plane-Wave Basis Set. *Phys. Rev. B: Condens. Matter Mater. Phys.* **1996**, *54*, 11169–11186.
- (45) Kresse, G.; Furthmüller, J. Efficiency of Ab-Initio Total Energy Calculations for Metals and Semiconductors Using a Plane-Wave Basis Set. *Comput. Mater. Sci.* **1996**, *6*, 15–30.
- (46) Kravchenko, P.; Plaisance, C.; Hibbitts, D. A New Computational Interface for Catalysis. **2019**, ChemRxiv.
- (47) Kresse, G.; Hafner, J. Ab Initio Molecular Dynamics for Liquid Metals. *Phys. Rev. B: Condens. Matter Mater. Phys.* **1993**, *47*, 558–561.
- (48) Kresse, G.; Hafner, J. Ab Initio Molecular-Dynamics Simulation of the Liquid-Metal–Amorphous-Semiconductor Transition in Germanium. *Phys. Rev. B: Condens. Matter Mater. Phys.* **1994**, *49*, 14251–14269.
- (49) Blöchl, P. E. Projector Augmented-Wave Method. *Phys. Rev. B: Condens. Matter Mater. Phys.* **1994**, *50*, 17953–17979.
- (50) Kresse, G.; Joubert, D. From ultrasoft pseudopotentials to the projector augmented-wave method. *Phys. Rev. B: Condens. Matter Mater. Phys.* **1999**, *59*, 1758–1775.
- (51) Hammer, B.; Hansen, L. B.; Nørskov, J. K. Improved Adsorption Energetics within Density-Functional Theory Using Revised Perdew-Burke-Ernzerhof Functionals. *Phys. Rev. B: Condens. Matter Mater. Phys.* **1999**, *59*, 7413–7421.
- (52) Kasper, J. S.; Lonsdale, K. *International Union of Crystallography, International Tables for X-Ray Crystallography*, 3rd ed.; Published for the International Union of Crystallography by D. Reidel Pub. Co.: Dordrecht; Boston, 1985.
- (53) Pack, J. D.; Monkhorst, H. J. Special Points for Brillouin-Zone Integrations - Reply. *Phys. Rev. B: Solid State* **1977**, *16*, 1748–1749.
- (54) Hibbitts, D. D.; Loveless, B. T.; Neurock, M.; Iglesia, E. Mechanistic Role of Water on the Rate and Selectivity of Fischer-Tropsch Synthesis on Ruthenium Catalysts. *Angew. Chem., Int. Ed.* **2013**, *52*, 12273–12278.
- (55) Almithn, A.; Hibbitts, D. Effects of Catalyst Model and High Adsorbate Coverages in Ab Initio Studies of Alkane Hydrogenolysis. *ACS Catal.* **2018**, *8*, 6375–6387.
- (56) McQuarrie, D. A. *Statistical Mechanics*; University Science Books: Sausalito, Calif., 2000.
- (57) Chen, B. W. J.; Mavrikakis, M. How Coverage Influences Thermodynamic and Kinetic Isotope Effects for H-2/D-2 Dissociative Adsorption on Transition Metals. *Catal. Sci. Technol.* **2020**, *10*, 671–689.
- (58) Karim, W.; Spreafico, C.; Kleibert, A.; Gobrecht, J.; VandeVondele, J.; Ekinici, Y.; van Bokhoven, J. A. Catalyst Support Effects on Hydrogen Spillover. *Nature* **2017**, *541*, 68–71.
- (59) Baró, A. M.; Ibach, H.; Bruchmann, H. D. Vibrational Modes of Hydrogen Adsorbed on Pt(111): Adsorption Site and Excitation Mechanism. *Surf. Sci.* **1979**, *88*, 384–398.
- (60) Collins, D. M.; Spicer, W. E. The Adsorption of Co, O₂, and H₂ on Pt: I. Thermal Desorption Spectroscopy Studies. *Surf. Sci.* **1977**, *69*, 85–113.
- (61) McCabe, R. W.; Schmidt, L. D. Binding States of Co and H₂ on Clean and Oxidized (111)Pt. *Surf. Sci.* **1977**, *65*, 189–209.
- (62) Hoffman, A. J.; Asokan, C.; Gadinis, N.; Kravchenko, P.; Getsoian, A. B.; Christopher, P.; Hibbitts, D. Theoretical and Experimental Characterization of Adsorbed Co and No on Γ -Al₂O₃-Supported Rh Nanoparticles. *J. Phys. Chem. C* **2021**, *125*, 19733–19755.
- (63) Liu, J.; Hibbitts, D.; Iglesia, E. Dense Co Adlayers as Enablers of Co Hydrogenation Turnovers on Ru Surfaces. *J. Am. Chem. Soc.* **2017**, *139*, 11789–11802.
- (64) Hibbitts, D.; Dybeck, E.; Lawlor, T.; Neurock, M.; Iglesia, E. Preferential Activation of Co near Hydrocarbon Chains During Fischer-Tropsch Synthesis on Ru. *J. Catal.* **2016**, *337*, 91–101.
- (65) Kravchenko, P.; Krishnan, V.; Hibbitts, D. Mechanism and Effects of Coverage and Particle Morphology on Rh-Catalyzed No–H₂ Reactions. *J. Phys. Chem. C* **2020**, *124*, 13291–13303.
- (66) Yik, E.; Hibbitts, D.; Wang, H.; Iglesia, E. Hydrogenation and Cs Bond Activation Pathways in Thiophene and Tetrahydrothiophene Reactions on Sulfur-Passivated Surfaces of Ru, Pt, and Re Nanoparticles. *Appl. Catal., B* **2021**, *291*, 119797.
- (67) Sato, S. Photoelectrochemical Preparation of Pt/TiO₂ Catalysts. *J. Catal.* **1985**, *92*, 11–16.
- (68) Kip, B.; Duivenvoorden, F. B. M.; Koningsberger, D. C.; Prins, R. Determination of Metal-Particle Size of Highly Dispersed Rh, Ir, and Pt Catalysts by Hydrogen Chemisorption and EXAFS. *J. Catal.* **1987**, *105*, 26–38.
- (69) Wanke, S.; Doughart, N. A. Interaction of Hydrogen, Oxygen, and Carbon-Monoxide with Supported Rhodium. *J. Catal.* **1972**, *24*, 367–384.
- (70) Mcvicker, G.; Ziemiak, J. J. Chemisorption Properties of Platinum and Iridium Supported on TiO₂-Al₂O₃ Mixed-Oxide Carriers - Evidence for Strong Metal Support Interaction Formation. *J. Catal.* **1985**, *95*, 473–481.

Recommended by ACS

The Extent of Platinum-Induced Hydrogen Spillover on Cerium Dioxide

Arik Beck, Jeroen A. van Bokhoven, *et al.*

DECEMBER 05, 2022

ACS NANO

READ 

Metal Encapsulation-Driven Strong Metal-Support Interaction on Pt/Co₃O₄ during CO Oxidation

Daeho Kim, Jeong Young Park, *et al.*

APRIL 05, 2023

ACS CATALYSIS

READ 

"Magic" Sinter-Resistant Cluster Sizes of Pt_n Supported on Alumina

Patricia Poths, Anastassia N. Alexandrova, *et al.*

NOVEMBER 22, 2022

THE JOURNAL OF PHYSICAL CHEMISTRY LETTERS

READ 

Kinetic Insights into the Tandem and Simultaneous Mechanisms of Propylene Epoxidation by H₂ and O₂ on Au-Ti Catalysts

Wei Du, Xingui Zhou, *et al.*

JANUARY 24, 2023

ACS CATALYSIS

READ 

Get More Suggestions >